Performance Evaluation of an Integrated Floating Energy System Based on Coupled Analysis

Yang YANG [a, b], Musa BASHIR [a], Jin WANG [a], Jie YU [b], Chun LI [b]

[a.] Department of Maritime and Mechanical Engineering, Liverpool John Moores University, Liverpool, Byrom Street, L3 3AF, UK

[b.] School of Energy and Power Engineering, University of Shanghai for Science and Technology, Shanghai, 200093, P.R. China

Abstract: An integrated floating energy system consisting of different types of energy devices is an ideal option for reducing the levelized cost of energy by enhancing the power production capacity. This study proposes a concept of an integrated energy system by combining two tidal turbines with a floating wind turbine. In order to investigate the power performance and dynamic responses of the hybrid concept, a novel coupled aero-hydro-servo-elastic tool is developed based on a commercial hydrodynamic analysis software package. In addition, a torque-pitch controller and the AeroDyn module are integrated within the coupled tool for evaluating the power performance of the tidal turbines under dynamic inflow conditions. Experimental data and numerical results obtained by OpenFAST are used to verify the accuracy of the coupled tool in predicting dynamic responses of the integrated energy system. The dynamic responses and power production under different environmental conditions are obtained by conducting a series of simulations. The results indicate that the total power production is increased by 3.84% to 6.46%. The transient behavior of the platform is improved and the tension fluctuation in mooring lines are significantly reduced by the hydrodynamic damping provided by the tidal turbines. In addition, the tidal turbines have no negative influences on the aero-elastic responses and power performance of the wind energy system. The results have demonstrated the advantages of the integrated energy system in enhancing the power production and improving the dynamic performance.

***Keywords*:** Integrated energy system; Floating wind turbine; Tidal turbine; Coupled model; Dynamic responses; Power production.

1 Introduction

Societal demand for improvements in climatic conditions requires the use of low emission energy sources to mitigate the greenhouse gases effect on the environment. Development of renewable energy resources offers the most efficient means of reducing carbon emissions resulting from the consumptions of fossil energy resources [1]. Offshore renewable energy resources are increasingly attracting attention to meet the growing demand of green energy development. Consequently, the floating energy technology has become a new theme of interest to academic research and commercial development due to the abundance of wind, wave and current resources in the deep sea areas.

Wind energy is the major contributor to the offshore energy development. The past decade has witnessed the conceptualization and commercial application of a number of floating platforms for wind energy exploration. Statoil developed a spar platform, the so-called Hywind concept [2], for the world's first full-scale large floating offshore wind turbine (FWT) with a capacity of 2.3 MW, which became operational in the North Sea, near Norway in 2009. The Hywind concept was adapted by the National Renewable Energy Laboratory (NREL) to support a 5 MW wind turbine in the Offshore Code Comparison Collaboration (OC3) project sponsored by the International Energy Agency (IEA) [3]. Due to its modelling simplicity and commercial viability, the OC3-Hywind was extensively used in a large number of studies in the development of floating wind technology. For instance, Karimirad and Moan [4] analyzed the global dynamic responses of a 5 MW wind turbine supported by a spar platform under harsh environmental and operating conditions. It was found that the dynamic and structural responses were independent of the wind turbulence. Ma *et al.* [5] employed a widely-used numerical analysis tool, FAST, to investigate the dynamic responses of the OC3-Hywind concept under different sea states. The spectral responses were presented to obtain a better understanding of the floating wind turbine's behaviour. Yue *et al.* [6] investigated the effects of heave plates on

the dynamic responses of the spar FWT using AQWA. It was found that the platform motion was affected by the vertical position of the heave plate. Ahn and Shin [7] conducted various experimental tests for the OC3-Hywind FWT with a 1/128 scale ratio. The model test results were compared with the predictions from an in-house code and FAST. It was observed that the numerical predictions of platform pitch were slightly larger than the test results. Lin *et al.* [8] investigated the hydrodynamic responses of the OC3-Hywind concept influenced by the mooring system that was modelled using a quasi-static method. The contributions of mooring loads to the platform motions were studied. Lyu *et al.* [9] investigated the effects of wind/wave incident directions of the OC3-Hywind platform responses. It was concluded that the wind/wave loads significantly affected the longitudinal modes of surge and pitch motions. In addition, NREL further developed a semi-submersible platform as an alternative floating wind system in the DeepCwind project [10]. In order to generate sufficient and valid experimental data for validating and improving the current numerical analysis methodologies for coupled modelling of FWTs, a series of model tests were conducted for the OC3-Hywind, semi-submersible and a tension leg platform (TLP) concepts [11]. Dynamic responses and fatigue damage of the blades and tower of the NREL 5 MW wind turbine supported by three different types of floating platforms were quantitatively compared [12].

Apart from the offshore wind resource, sea current is also increasingly attracting attention as an alternative sustainable resource for electricity production. Similar to the wind energy devices, the most popular design concept of current/tidal turbines is the horizontal axis form [13]. Patel *et al.* [14] conducted experimental tests to investigate the hydrodynamic performance of various Darrieus turbines. The solidity effect on the power performance of the hydrokinetic turbines was studied. It was found that the power coefficient of the turbines with a symmetric aerofoil achieved their peak at a solidity close to 0.38. In addition, Patel *et al.* [15] conducted an experimental study to enhance the hydrodynamic performance of a Darrieus

turbine using a blocking plate. The width and location of the blocking plate were tested. The power coefficient of the tidal turbine was increased from 0.125 to 0.36 using an optimal blocking plate. Blackmore *et al.* [16] investigated the effect of turbulence on the power performance and fatigue loads on blades of a tidal turbine through experimental tests. The experiments indicated that the thrust and torque of the tidal turbine were significantly influenced by the dynamic inflow velocity. Scarlett *et al.* [17] carried out a parametric study for a range of flow conditions to investigate the unsteady hydrodynamic performance of tidal turbine blades. It was found that load fluctuations from the blades increased due to a yaw misalignment. Bahaj [18] compared the numerical results obtained using a commercial code with the experimental data. The comparison indicated that the blade element momentum (BEM) theory was able to produce satisfactory representations of the experimental turbine's performance. Zhang *et al.* [19] investigated the hydrodynamic performance of a tidal turbine which was attached on a floating platform. The numerical results indicated that the surge motion had a significant influence on the dynamic performance of the tidal turbine. Patel *et al.* [20] studied the effect of overlap ratio and aspect ratio on the performance of a Savonius-type hydrokinetic turbine through experimental tests. The best overlap and aspect ratios were specified for the purpose of obtaining a maximum energy harvesting efficiency. Patel *et al.* [21] developed a theory based on stagnation pressure and impulse momentum principle for estimating the hydrodynamic performance of a Savonius turbine. The numerical predictions were compared with the data from experimental tests for the validation.

In deep sea areas where wind and current resources coexist, a hybrid energy system consisting of a FWT and several tidal turbines is a prospective and feasible solution to reducing the levelized cost of electricity (LCoE) by sharing the support system. A number of studies have been conducted to investigate the dynamic responses and power production of a hybrid floating energy system. Muliawan *et al.* [22] investigated the dynamic responses and power

performance of a combined spar FWT and coaxial floating wave energy converter (WEC) using SIMO/TDHMILL3D. The power take-off system between the WEC and spar platform was modelled as a simple spring-damper. The numerical simulation results of the combined concept under several operating conditions indicated that the fluctuations in the platform motions decreased. The total output power increased by 6% to 15% depending on the environmental conditions. Wan *et al.* [23] conducted an experimental study on the same model under survival conditions to further confirm the deployment feasibility of the combined concept. The test results conformed the accuracy of the numerical modelling in predicting the dynamic responses. A slamming model was suggested to be added into the numerical model to consider the slamming effects which were observed in the tests. Michailides *et al.* [24] studied the dynamic responses and functionality of a semi-submersible wind turbine combined with flap-type wave energy converters through experimental tests and numerical analysis. The results indicated that the combined concept performed well in extreme environmental conditions and no strong nonlinear phenomena were produced [25]. Michele *et al.* [26] developed a mathematical model to study the hydrodynamics of a hybrid wind-wave energy system. The power production capabilities of the hybrid system in regular and irregular wave conditions were investigated. Hallak *et al.* [27] numerically and experimentally analyzed the performance of a combined concept composed of a semi-submersible wind platform and a number of oscillating wave columns. It was found that the hybrid concept benefitted with stability enhancement and smoother energy output. Li *et al.* [28] investigated the dynamic response and power production of a floating energy system consisting of wind, wave and tidal energy devices. It was found that the overall power production increased compared to a single FWT. In addition, the transient behavior following an emergency shutdown was more moderate due to the presence of wave and tidal energy systems. The short-term [29] and long-term [30] extreme responses of the integrated energy system were further studied. It was found that the fatigue damage of

mooring lines increased. However, the elasticity of the flexible elements including the blades and tower of the wind turbine was ignored in modelling the hybrid energy system. Moreover, no servo-control scheme was applied to adjust the blade-pitch and rotor speed when evaluating the power production in their studies. It is apparent that the dynamic responses and power performance of such an integrated energy system have not been adequately evaluated.

In order to more accurately investigate the dynamic responses and power performance of an integrated floating energy system (IFES), this study has developed a fully coupled aero-hydro-servo-elastic tool based on a commercial hydrodynamic analysis software package, AQWA. The examined IFES concept is composed of a 5 MW spar-type FWT and two 550 kW tidal turbines. In addition, the AeroDyn module developed by NREL is integrated within the coupled tool to predict the hydrodynamic forces produced by the tidal turbines. The influence of platform motions on the relative current speed is considered. The accuracy of the fully coupled tool in predicting dynamic responses of the FWT and tidal turbine is validated through comparisons against OpenFAST and experimental tests, respectively. The coupled dynamic responses of the blades, platform and mooring lines of the IFES under below-rated, rated and over-rated operating conditions are obtained and compared with those of a single FWT. The power production capacity of the IFES is also evaluated to confirm the benefits produced by integrating the tidal turbines with a wind energy system.

2 Description of the integrated floating energy system

The IFES model proposed in this study is composed of the NREL 5 MW wind turbine [31] and two identical tidal turbines. Both the wind turbine and tidal turbines are integrated on the spar platform as shown in Fig. 1.

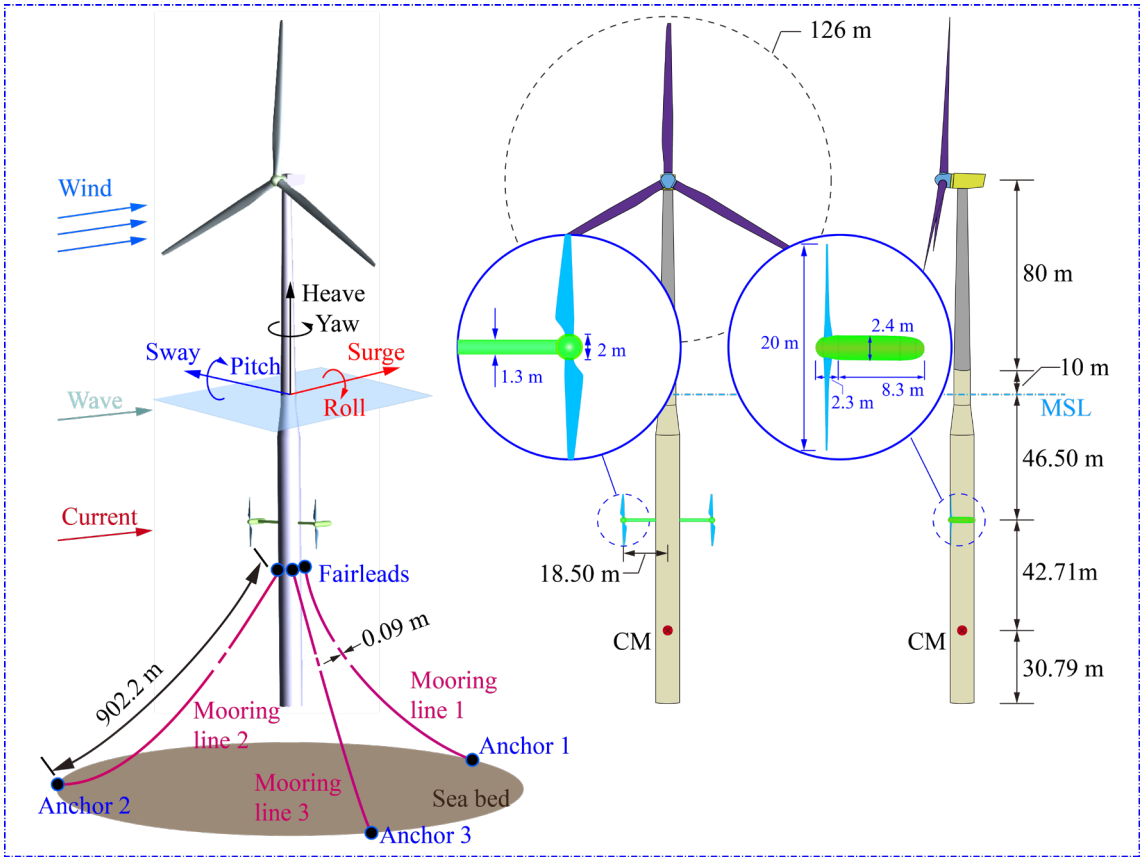

Fig. 1: Schematic diagram of the integrated floating energy system

The extensively-used OC3-Hywind spar [3] is chosen as the main floating component of the IFES concept. The design water depth and total draft of the spar are 320 m and 120 m, respectively. The geometry of the spar near the free-surface is tapered to facilitate a better connection with the tower of the wind turbine. The diameters of the spar above and below the taper are 6.5 m and 9.4 m, respectively. A mooring system consisting of three catenary lines is used for the station-keeping of the platform. The fairleads are attached on the platform at 70 m water depth and the radius of the anchors is 853.87 m. The unstretched length and mass density of each mooring line are 902.2 m and 77.7 kg/m, respectively. The axial stiffness and equivalent weight in water of each mooring line are 384,243,000 N and 698.094 N/m, respectively. The additional yaw stiffness provided by the mooring system is 9.834×10^{7}Nm/rad.

The tidal turbine was designed by the Sandia National Laboratory for the development of

168 marine hydrokinetic technology [32]. The diameters of the rotor and hub are 20 m and 2 m,
169 respectively. The NACA 63-424 aerofoil was used to design the hydrodynamic shape of the
170 rotor blades through an optimization tool named HARP_Opt tool. In this study, the rated rotor
171 speed is increased from 11.5 rpm to 13 rpm to achieve the design power of 550 kW under the
172 rated current speed of 2.0 m/s. Main specifications of the tidal turbine are presented in Table 1
173 and the hydrodynamic shape of the blade is presented in Table 2.

174 Table 1: Main specifications of the tidal turbine [32]

Property	**Value**	**Unit**
Rated power	550	kW
Cut-in/cut-out current speed	0.5/3.0	m/s
Cut-in/rated rotor speed	3.0/13.0	rpm
Diameter of the rotor	20.0	m
Diameter of the hub	2.0	m
Rotor mass	1200	kg
Nacelle mass	40,100	kg
Cross-beam mass	20,000	kg
Drivetrain inertia moment	4.44×10^6	$kg\cdot m^2$
Depth to hub below MSL	46.5	m
Distance to hub from centreline of the platform	18.5	m

175 Table 2: Hydrodynamic shape of the tidal turbine blade [32]

Local radius (m)	**Aerofoil (-)**	**Twist (deg)**	**Chord (m)**	**Relative thickness (%)**
1.00	Cylinder	12.86	0.800	100.00
1.89	Interpolated	12.86	1.243	53.30
2.70	Interpolated	12.79	1.702	27.55
3.55	NACA 63-424	9.50	1.577	24.00
4.23	NACA 63-424	7.85	1.481	24.00
5.01	NACA 63-424	6.51	1.371	24.00
5.84	NACA 63-424	5.47	1.251	24.00
6.62	NACA 63-424	4.71	1.138	24.00
7.23	NACA 63-424	4.20	1.046	24.00
7.89	NACA 63-424	3.69	0.945	24.00
8.45	NACA 63-424	3.28	0.856	24.00
8.92	NACA 63-424	2.92	0.781	24.00
9.24	NACA 63-424	2.68	0.728	24.00
9.64	NACA 63-424	2.35	0.661	24.00
10.00	NACA 63-424	2.10	0.600	24.00

176

177 As indicated in Fig. 1, the tidal turbines are placed at a water depth of 46.5 m. The distance

between the tidal turbine's hub and the platform's centerline is 18.5 m. The weight of each tidal turbine including the nacelle and the connecting beam is 6.13×10^4 kg. The added inertial moments of the platform due to the tidal turbines are calculated. By assuming that the ballast of the platform remains unchanged when integrated with the tidal turbines, the inertial properties of the platform are given in Table 3.

Table 3: Inertial properties of the platform with the tidal turbines

Property	**Value**	**Unit**
Platform mass (with tidal turbines)	7,588,930	kg
Centre of mass (CM) below MSL	89.2141	m
Platform roll inertia about CM	4.46032×10^9	$kg\cdot m^2$
Platform pitch inertia about CM	4.46032×10^9	$kg\cdot m^2$
Platform yaw inertia about CM	1.68822×10^8	$kg\cdot m^2$

3 Aero-hydro-servo-elastic modelling of the hybrid concept

In order to obtain the dynamic responses of the IFES subjected to wind, wave and current loadings as realistic as possible, an aero-hydro-servo-elastic coupled tool is developed in this study based on a commercial hydrodynamic analysis software tool, AQWA. The aero-servo-elastic simulation capability is implemented within the *user_force64.dll*, which is invoked by the AQWA solver at each time step during a time domain analysis. The kinematics and kinetics of the wind turbine are temporarily stored in the DLL to be used for the simulation in the next time step. The loads calculated by the DLL are coupled with hydrodynamic loads and mooring restoring forces to address the dynamics of the platform and mooring system in the AQWA solver. In addition, the hydrodynamic load of each tidal turbine is calculated using AeroDyn through the DLL, while the dynamic inflow effects due to platform motions are considered. The methodologies used for the development of the aero-hydro-servo-elastic coupled model of the IFES concept are described subsequently. Fig. 2 presents a flowchart of the fully coupled aero-hydro-servo-elastic model established in AQWA. It is apparent that the platform responses obtained using the AQWA solver are influenced by the responses of the wind turbine

and tidal turbines predicted in the *user_force64.dll*, and vice versa.

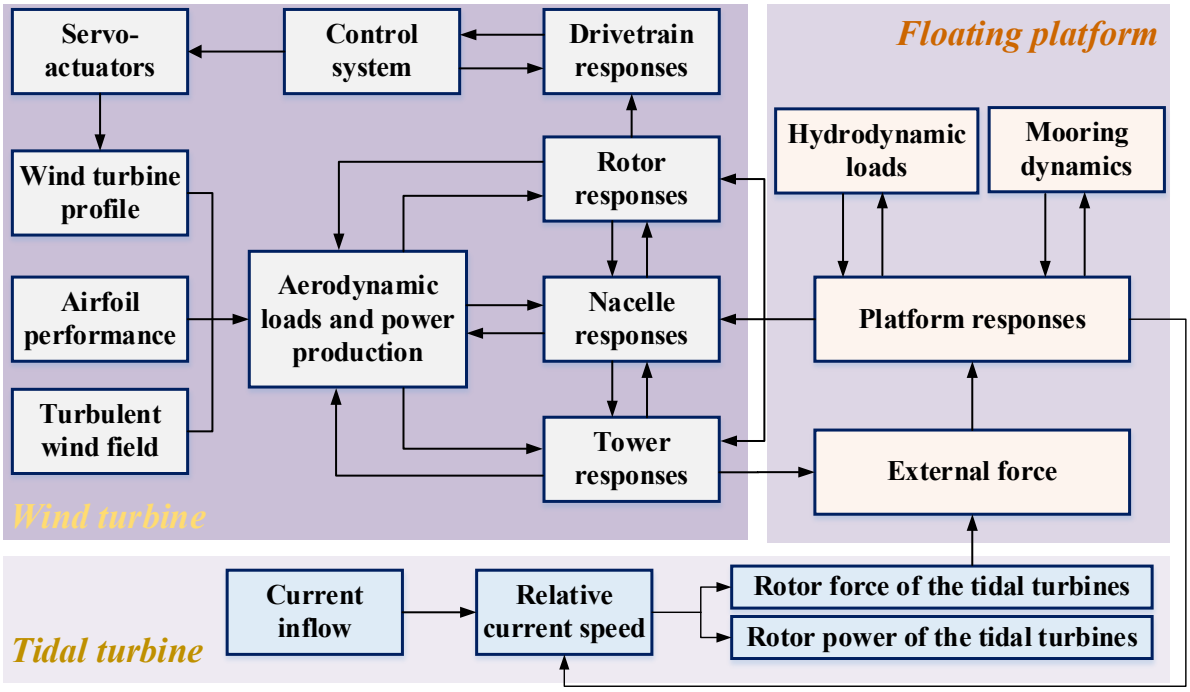

Fig. 2: Flowchart of the fully coupled model for an integrated floating energy system

3.1 Aerodynamic modelling of the rotor

The general dynamic wake (GDW) model and blade element momentum (BEM) [33] theory are adopted to predict the aerodynamic loads of the wind turbine and the hydrodynamic loads of the tidal turbine under a dynamic inflow condition. In the GDW model, the induced velocities and pressure over the rotor disk are solved based on the potential flow theory. By expressing the pressure and induced velocity as infinite series of sines and cosines, the governing equations of the GDW model in the axial and tangential directions are derived in Eq. (1) and Eq. (2), respectively [34].

$$\left[\boldsymbol{M}^{C}\right]\left\{\begin{matrix}\vdots\\ \left\{\alpha_{\mathrm{j}}^{\mathrm{h}}\right\}\\ \vdots\end{matrix}\right\}^{*}+\left[\tilde{\boldsymbol{L}}^{C}\right]^{-1}\left[\hat{\boldsymbol{V}}^{C}\right]\left\{\begin{matrix}\vdots\\ \left\{\alpha_{\mathrm{j}}^{\mathrm{h}}\right\}\\ \vdots\end{matrix}\right\}=\frac{1}{2}\left\{\begin{matrix}\vdots\\ \left\{\tau_{\mathrm{n}}^{\mathrm{m}C}\right\}\\ \vdots\end{matrix}\right\} \tag{1}$$

$$\left[\boldsymbol{M}^{S}\right]\left\{\begin{array}{c}\vdots\\ \left\{\beta_{\mathrm{j}}^{\mathrm{h}}\right\}\\ \vdots\end{array}\right\}^{*}+\left[\tilde{\boldsymbol{L}}^{S}\right]^{-1}\left[\hat{\boldsymbol{V}}^{S}\right]\left\{\begin{array}{c}\vdots\\ \left\{\beta_{\mathrm{j}}^{\mathrm{h}}\right\}\\ \vdots\end{array}\right\}=\frac{1}{2}\left\{\begin{array}{c}\vdots\\ \left\{\tau_{\mathrm{n}}^{\mathrm{m}S}\right\}\\ \vdots\end{array}\right\} \tag{2}$$

where $[\boldsymbol{M}^{C}]$ and $[\boldsymbol{M}^{S}]$ are the cosine and sine terms of the apparent mass matrix $[\tilde{\boldsymbol{M}}]$, respectively. $[\tilde{\boldsymbol{L}}^{C}]$ and $[\tilde{\boldsymbol{L}}^{S}]$ are the cosine and sine components of the matrix of inflow gain, respectively. $[\hat{\boldsymbol{V}}^{C}]$ and $[\hat{\boldsymbol{V}}^{S}]$ are the cosine and sine terms of the flow parameters, respectively. $\tau_{\mathrm{n}}^{\mathrm{m}C}$ and $\tau_{\mathrm{n}}^{\mathrm{m}S}$ are respectively the axial and tangential coefficients of dimensionless pressure. $\alpha_{\mathrm{j}}^{\mathrm{h}}$ and $\beta_{\mathrm{j}}^{\mathrm{h}}$ are respectively the axial and tangential coefficients of induced velocity.

The induced velocity distribution over the rotor disk is obtained by solving the above differential equations. The Prandtl corrections are used to consider the tip and hub losses. The BEM theory is then used to calculate the loads acting on each blade element based on the lift and drag coefficients of the local sectional aerofoil, as denoted in Eq. (3) and Eq. (4) [35].

$$\mathrm{d}T=\frac{1}{2}\rho W^{2}c(C_{l}\cos\phi+C_{d}\sin\phi)\mathrm{d}r \tag{3}$$

$$\mathrm{d}M=\frac{1}{2}\rho W^{2}c(C_{l}\sin\phi-C_{d}\cos\phi)r\mathrm{d}r \tag{4}$$

where dT and dM are, respectively, the thrust and moment of the local blade element; ρ is the density of the inflow fluid; C_{l} and C_{d} are, respectively, the lift and drag coefficients of the sectional aerofoil; The Beddoes-Leishman dynamic stall model is used to correct the aerodynamic coefficients under unsteady conditions; c is the chord length of the blade element; r and dr are the local radius and length of the blade element, respectively; ϕ is the relative inflow angle of the local section; W denotes the relative inflow speed.

3.2 Structural modelling of the wind turbine

The wind turbine is modelled as a multi-body system consisting of rigid and flexible

bodies. The hub and nacelle were treated as rigid bodies. The tower and blades were modelled as flexible bodies based on the linear modal approach. For each blade, two flapwise and one edgewise modes are considered. The first two modes in the fore-aft and side-side directions are examined for the tower. In addition, the nacelle-yaw and rotation of the drivetrain system are accounted in the simulation. Kane's method [36] is used to establish the equations of motion of the wind turbine, as follows:

$$\boldsymbol{F}_i^* + \boldsymbol{F}_i = 0 \tag{5}$$

where $\boldsymbol{F}_i^*$ and $\boldsymbol{F}_i$ are the generalized inertia and active forces corresponding to the i^{th} degree of freedom (DOF) of the wind turbine.

The generalized inertia force of a rigid body can be represented using the same formula. For instance, the generalized inertia force of the nacelle $\boldsymbol{F}_{\text{Nac}}^*$ is derived as:

$$\boldsymbol{F}_{\text{Nac}}^* = \sum_{i=1}^{N} v_{i,\text{Nac}}(-m_{\text{Nac}} \cdot a_{\text{Nac}}) + \omega_i(-\dot{H}_{\text{Nac}}) \tag{6}$$

where N is the number of total examined DOFs of the wind turbine; $v_{i,\text{Nac}}$ is the partial velocity of the nacelle contributed by the i^{th} DOF of the wind turbine; m_{Nac} and a_{Nac} are respectively the mass and acceleration of the nacelle; ω_i is the partial angular velocity of the nacelle contributed by the i^{th} DOF of the wind turbine; $\dot{H}_{\text{Nac}}$ is the time derivative of angular momentum of the nacelle about its mass center.

The term, $\omega_i(-\dot{H}_{\text{Nac}})$, denotes the gyroscopic yaw moment induced by the spinning inertia and pitching motion of the rotor. The pitching motion denoted by the partial angular velocity (ω_i) is influenced by the pitching velocities of the tower and platform. An exhaustive description of the relationship between the partial angular velocity of the nacelle and kinematics of tower and platform is beyond the scope of this study. Further details can be found in reference [36]

The generalized inertia force of a blade $\boldsymbol{F}_{\text{Bld}}^*$ is denoted as:

$$\boldsymbol{F}_{\mathrm{Bld}}^{*}=-\sum_{i=1}^{N}\int_{0}^{R_{\mathrm{rt}}-R_{\mathrm{hub}}}\rho_{\mathrm{Bld}}(r)\cdot v_{i,\mathrm{Bld}}(r)\cdot a_{\mathrm{Bld}}(r)\cdot \mathrm{d}r \tag{7}$$

where R_{rt} and R_{hub} are the radii of the rotor and hub, respectively; $\rho_{\mathrm{Bld}}(r)$ is the mass of the blade per unit length; $v_{i,\mathrm{Bld}}(r)$ is the partial velocity of the local blade section contributed by the i^{th} DOF of the wind turbine; and $a_{\mathrm{Bld}}(r)$ is the acceleration of the local blade section.

The generalized active forces are composed of aerodynamic load $F_{i,\mathrm{aero}}$, elastic restoring force $F_{i,\mathrm{elastic}}$, gravitational load $F_{i,\mathrm{grav}}$ and damping force $F_{i,\mathrm{damp}}$, as denoted in Eq. (8).

$$F_i = F_{i,\mathrm{aero}}+F_{i,\mathrm{elastic}}+F_{i,\mathrm{grav}}+F_{i,\mathrm{damp}} \tag{8}$$

The generalized active aerodynamic force acting on a blade $F_{\mathrm{Bld,aero}}$ is denoted as:

$$F_{\mathrm{Bld,aero}}=\sum_{i=1}^{N}\int_{0}^{R_{\mathrm{rt}}-R_{\mathrm{hub}}}v_{i,\mathrm{Bld}}(r)\cdot F_{\mathrm{aero}}(r)\cdot \mathrm{d}r \tag{9}$$

where $F_{\mathrm{aero}}(r)$ is the total force acting on the local blade section.

The generalized active elastic restoring force of a blade is defined as a partial derivative of the potential energy with respect to the generalized coordinate, as follows:

$$F_{\mathrm{Bld,elastic}}=\frac{\partial V_{\mathrm{PE}}}{\partial q_{\mathrm{Bld}}}=\frac{\partial\left[\frac{1}{2}\sum_{i}^{n}\sum_{j}^{n}k_{ij}\cdot q_i(t)\cdot q_j(t)\right]}{\partial\left[q_{\mathrm{Bld}}(t)\right]} \tag{10}$$

where V_{PE} is the potential energy of the blade; $q_i(t)$ is the generalized coordinate associated with the i^{th} mode pertaining to the blade at the time of t; n is the number of the examined modes of the blade; k_{ij} is the generalized stiffness of the blade and its value is zero when $i \neq j$.

Considering rotational effects of the rotor, the generalized stiffness of a blade is given in Eq. (11).

$$k_{ij}=\int_{0}^{R_{\mathrm{rt}}-R_{\mathrm{hub}}}EI_{\mathrm{Bld}}(r)\frac{\mathrm{d}^2\varphi_i(r)}{\mathrm{d}r^2}\frac{\mathrm{d}^2\varphi_j(r)}{\mathrm{d}r^2}\mathrm{d}r+k_{\mathrm{tm},ij}+k_{\mathrm{lm},ij} \tag{11}$$

where $EI_{\mathrm{Bld}}(r)$ is the distributed stiffness of the blade. $\varphi_i(r)$ is the i^{th} normalized modal shape of the blade; $k_{\mathrm{tm},ij}$ and $k_{\mathrm{lm},ij}$ are the generalized stiffness due to the tip mass and local mass of the blade, as derived in Eq. (12) and Eq. (13), respectively.

$$k_{\mathrm{tm},ij} = \Omega^2 m_{\mathrm{tip}} R_{\mathrm{rt}} \int_0^{R_{\mathrm{rt}}-R_{\mathrm{hub}}} \frac{\mathrm{d}\varphi_i(r)}{\mathrm{d}r} \frac{\mathrm{d}\varphi_j(r)}{\mathrm{d}r} \mathrm{d}r \tag{12}$$

$$k_{\mathrm{lm},ij} = \Omega^2 \int_0^{R_{\mathrm{rt}}-R_{\mathrm{hub}}} \rho_{\mathrm{Bld}}(r)(R_{\mathrm{rt}}+r) \left[\int_0^r \frac{\mathrm{d}\varphi_i(r')}{\mathrm{d}r'} \frac{\mathrm{d}\varphi_j(r')}{\mathrm{d}r'} \mathrm{d}r' \right] \mathrm{d}r \tag{13}$$

where Ω and m_{tip} are the rotational speed of the rotor and the tip mass of the blade, respectively.

Substituting Eqs. (6)~(13) into Eq. (5), the coupled equation of motion of the wind turbine is established. It is noted that the effects of platform motions on the kinematics of the upper structures including the rotor, nacelle and tower are considered based on the theory described in [37] when solving Eq. (5) in the DLL. The kinetic results obtained from the solutions are passed into AQWA solver through the DLL for the calculation of platform motions at each time step in the analysis. The platform's kinematics obtained from the AQWA solver are then fed back into the DLL for solving Eq. (5) at the next time step.

3.3 Integration of the coupled model of the IFES

The aero-servo-elastic model is integrated within a commercial hydrodynamic analysis tool, AQWA, through its built-in DLL (*user_force64.dll*) to form a fully coupled model of IFES. In a time-domain analysis performed in AQWA, the DLL is invoked by the AQWA solver to obtain the external force and added-mass. The aero-servo-elastic simulation capability is implemented within the DLL by fully modifying its source code. The aero-servo-elastic responses of the upper structures are represented by the external force and added-mass during each invocation, and then passed into AQWA solver to be combined with the hydrodynamic loads and mooring restoring forces for obtaining the dynamic responses of the platform. The equation of motion of the platform is derived as follows:

$$(\boldsymbol{m} + \boldsymbol{A}_{\mathrm{wv}} + \boldsymbol{A}_{\mathrm{wt}})\ddot{\boldsymbol{X}}(t) + \boldsymbol{C}\dot{\boldsymbol{X}}(t) + \boldsymbol{K}\boldsymbol{X}(t) + \int_0^t \boldsymbol{h}(t-\tau)\ddot{\boldsymbol{X}}(\tau)\mathrm{d}\tau = \boldsymbol{F}_{\mathrm{h}}(t) + \boldsymbol{F}_{\mathrm{t}}(t) + \boldsymbol{F}_{\mathrm{e}}(t) \tag{14}$$

where $\boldsymbol{m}$ is the inertial mass matrix of the platform, $\boldsymbol{A}_{\mathrm{wv}}$ is the added-mass matrix due to the wave, $\boldsymbol{A}_{\mathrm{wt}}$ is the mass matrix of the upper structures referred to the platform's mass center; $\boldsymbol{K}$ and $\boldsymbol{C}$ are, respectively, the total stiffness and damping matrices; $\boldsymbol{X}(t)$, $\dot{\boldsymbol{X}}(t)$ and $\ddot{\boldsymbol{X}}(t)$ are, respectively, the displacement, velocity and acceleration vectors of the platform; $\boldsymbol{h}(t)$ is the acceleration impulse function matrix used to examine the radiation memory effects; $\boldsymbol{F}_{\mathrm{h}}(t)$ and $\boldsymbol{F}_{\mathrm{t}}(t)$ are, respectively, the total hydrodynamic and mooring load vectors acting on the platform; $\boldsymbol{F}_{\mathrm{e}}(t)$ is the external force vector obtained through the DLL, including the loads from the upper structures and the force acting on the tidal turbine.

The hydrodynamic loads acting on the platform are calculated based on the frequency-dependent hydrodynamic coefficients including the added mass, radiation damping and restoring forces, which are obtained from a frequency domain analysis in AQWA. The panel model of the IFES is presented in Fig. 3. Since the blades of the tidal turbines are small components but with a complicated geometry, they have been represented by an equivalent diameter cylinder for simplicity in performing the frequency domain analysis.

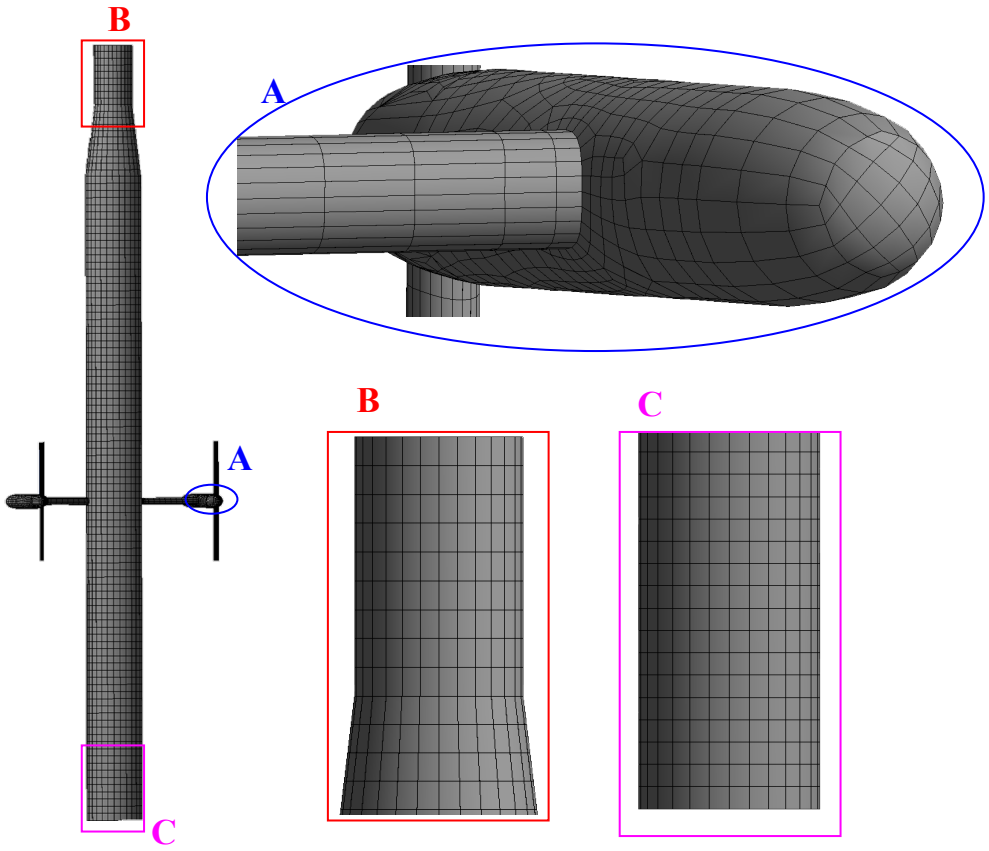

318

319 Fig. 3: Panel model of the integrated floating energy system in AQWA

320

321 The hydrodynamic force acting on the tidal turbine's rotating rotor due to the inflow
322 current is calculated using AeroDyn. The interaction between the tidal turbines and the
323 platform is examined by considering the relative inflow effects due to the platform motions. In
324 other words, the longitudinal velocity of the tidal turbine is affected by the platform surge,
325 pitch and yaw motion as shown in Fig. 4.

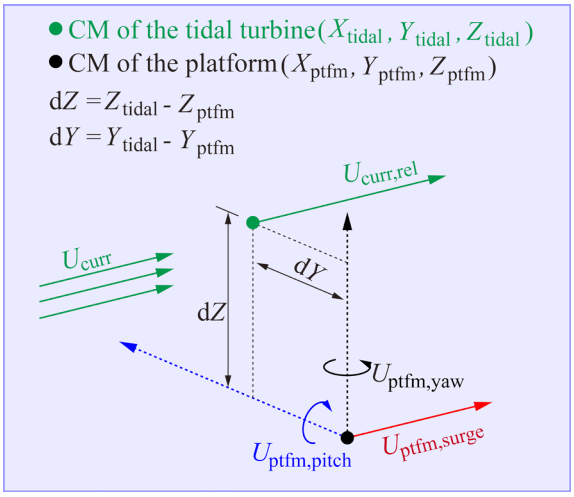

Fig. 4: Velocities of the tidal turbine and platform

Based on the assumption of small rotations of the platform, the actual relative inflow current speed $U_{curr,rel}$ is corrected as follows:

$$U_{curr,rel} = U_{curr} - U_{ptfm,surge} - (Z_{tidal} - Z_{ptfm})U_{ptfm,pitch} + (Y_{tidal} - Y_{ptfm})U_{ptfm,yaw} \quad (15)$$

where U_{curr} is the defined inflow current speed at the tidal hub depth. $U_{ptfm,surge}$, $U_{ptfm,pitch}$ and $U_{ptfm,yaw}$ are the surge, pitch and yaw velocities of the platform, respectively. Z_{tidal} and Z_{ptfm} are the vertical coordinates of the CMs of the tidal turbine and platform, respectively. Y_{tidal} and Y_{ptfm} are the lateral coordinates of the CMs of the tidal turbine and platform, respectively.

The current speed along water depth follows a power law distribution with an exponent of 1/7. At each time step, U_{curr} is calculated according to the hub depth of the tidal turbine and the given current speed at the MSL. A variable-speed and variable-pitch controller is implemented based on the control algorithm proposed by Jonkman [31] for the NREL 5MW wind turbine. The power and torque performance of the tidal turbine subjected to different steady inflow current speeds are evaluated in order to obtain the proportional and integral gains. Appendix A presents a brief description of the implementation method of the controller for the

tidal turbine.

It is noted that the results directly produced by the AQWA solver and the DLL are referred to different coordinate systems. The tower-base loads referred to the platform's local coordinate system need to be converted to the external force referred to the inertial coordinate frame. In addition, the external forces are applied at the platform's CM. Similarly, the platform motions used to correct the kinematics of the blades and tower need to be converted from the inertia coordinate system to its local coordinate frame. The matrix, $\mathbf{T}_{\text{mat}}$, given in Eq. (16) is used to achieve accurate transformations on the platform kinematics and external forces.

$$\mathbf{T}_{\text{mat}} = \begin{bmatrix} \dfrac{\theta_1^2\sqrt{1+s}+\theta_2^2+\theta_3^2}{s\sqrt{1+s}} & \dfrac{\theta_3 s+\theta_1\theta_2(\sqrt{1+s}-1)}{s\sqrt{1+s}} & \dfrac{-\theta_2 s+\theta_1\theta_3(\sqrt{1+s}-1)}{s\sqrt{1+s}} \\ \dfrac{-\theta_3 s+\theta_1\theta_2(\sqrt{1+s}-1)}{s\sqrt{1+s}} & \dfrac{\theta_2^2\sqrt{1+s}+\theta_1^2+\theta_3^2}{s\sqrt{1+s}} & \dfrac{\theta_1 s+\theta_2\theta_3(\sqrt{1+s}-1)}{s\sqrt{1+s}} \\ \dfrac{\theta_2 s+\theta_1\theta_3(\sqrt{1+s}-1)}{s\sqrt{1+s}} & \dfrac{-\theta_1 s+\theta_2\theta_3(\sqrt{1+s}-1)}{s\sqrt{1+s}} & \dfrac{\theta_3^2\sqrt{1+s}+\theta_1^2+\theta_2^2}{s\sqrt{1+s}} \end{bmatrix} \tag{16}$$

where θ_1, θ_2 and θ_3 are, respectively, the roll, pitch and yaw angles of the platform. s is equal to $\theta_1^2+\theta_2^2+\theta_3^2$.

By setting the platform reference point as the origin of the inertial coordinate system in establishing its local coordinate frame, the platform position vector is corrected as follows:

$$\mathbf{D}_{\text{DLL}} = \mathbf{D}_{\text{AQWA}} - \mathbf{T}_{\text{mat}} \cdot \mathbf{CoG} \tag{17}$$

where $\mathbf{CoG}$ is the position vector from the reference point to the platform's CM. $\mathbf{D}_{\text{AQWA}}$ and $\mathbf{D}_{\text{DLL}}$ are the platform displacement vectors obtained in AQWA and the one passed into the DLL, respectively.

The translational velocity vector of the platform is corrected as follows:

$$\mathbf{U}_{\text{DLL}} = \mathbf{U}_{\text{AQWA}} - \mathbf{T}_{\text{mat}} \cdot \mathbf{CoG} \times \boldsymbol{\omega} \tag{18}$$

where $\mathbf{U}_{\text{AQWA}}$ and $\mathbf{U}_{\text{DLL}}$ are the platform velocity vectors obtained in AQWA and the one

used in the DLL, respectively; $\boldsymbol{\omega}$ is the rotational velocity vector of the platform obtained in AQWA.

Since the fourth-order Adams-Beshforth-Mounton predictor-corrector method is used to solve the equation of motion given in Eq. (5), the accelerations of the involved structures are needed. However, the platform acceleration is not permitted to be shared with the DLL. Therefore, the platform acceleration vector is estimated numerically in the DLL based on the velocity vectors at the last and current time steps as follows:

$$\mathbf{a}_{\mathrm{DLL}} = (\mathbf{U}_{\mathrm{DLL}} - \mathbf{U}'_{\mathrm{DLL}})/\Delta t \tag{19}$$

where $\mathbf{a}_{\mathrm{DLL}}$ is the platform acceleration and $\mathbf{U}'_{\mathrm{DLL}}$ is the platform velocity at the last time step, Δt is the time step of the simulation.

Similarly, the tower-base loads obtained directly in the DLL are transformed as follows:

$$\mathbf{F}_{\mathrm{AQWA}} = \mathbf{T}_{\mathrm{mat}}^{-1} \cdot \mathbf{F}_{\mathrm{DLL}} \tag{20}$$

$$\mathbf{M}_{\mathrm{AQWA}} = \mathbf{T}_{\mathrm{mat}}^{-1} \cdot (\mathbf{M}_{\mathrm{DLL}} - \mathbf{CoG} \times \mathbf{F}_{\mathrm{DLL}}) \tag{21}$$

where $\mathbf{F}_{\mathrm{AQWA}}$ and $\mathbf{F}_{\mathrm{DLL}}$ are the translational force vectors in the AQWA program and DLL, respectively. $\mathbf{T}_{\mathrm{mat}}^{-1}$ is the inverse matrix of $\mathbf{T}_{\mathrm{mat}}$. $\mathbf{M}_{\mathrm{AQWA}}$ used in AQWA is the moment vector acting at the platform's mass center with respect to the inertial coordinate system. $\mathbf{M}_{\mathrm{DLL}}$ obtained in the DLL is the moment vector acting at the tower-base with respect to the platform's local coordinate system.

4 Validation of the fully coupled model

Since there is no credible model test or numerical data available for the full IFES model adopted in this study, the validation of the aero-hydro-servo-elastic coupled model is conducted in two parts: (i) to validate the accuracy of the fully coupled model in predicting dynamic

387 responses of a FWT by comparing it with OpenFAST; (ii) to confirm that hydrodynamic
388 performance of a tidal turbine can be evaluated credibly; the results from the model tests by
389 Bahaj *et al.* [38] and Doman *et al.* [39] are used in the comparisons. In addition, the results of
390 the tidal turbine under steady inflow conditions are compared with its design parameters to
391 verify the controller.

392 ### *4.1 Accuracy in predicting fully coupled responses of the wind turbine*

393 FAST was developed by NREL for aero-hydro-servo-elastic coupled analysis of
394 horizontal axis wind turbines. FAST has been verified and approved as credible numerical tool
395 for the analysis of wind-wave coupled loads on wind turbines by Germanischer Lloyd. In
396 addition, FAST was used as the main numerical tool in numerous international projects
397 including the OC3 project, a collaborative research with focus on validation and improvement
398 of numerical tools for wind turbine analysis. The numerical predictions from FAST agreed well
399 with the experimental data for the OC3-Hywind [40] and DeepCwind semi-submersible [41]
400 concepts. Since FAST has been well validated by experimental data in numerous studies, it is
401 agreed that the tool is capable of producing accurate and reliable numerical results for
402 simulations of FWTs under wind-wave coupled conditions. OpenFAST, the latest version of
403 FAST, is therefore used to validate the coupled model developed in this study.

404 Since the process of generating an irregular wave in AQWA and OpenFAST is different,
405 the examined met-ocean condition is composed of a regular wave and a turbulent wind. The
406 turbulent wind has an average speed of 11.4 m/s at the hub height and a shear exponent of 0.12.
407 The wave height and period are, respectively, 1.94 m and 5.01 s. The coupled responses of the
408 platform are compared in Fig. 5. Although a notable difference is observed, the platform surge
409 motion predicted by the coupled model in AQWA follows the same trend as the results obtained
410 using OpenFAST. The average surge motions of AQWA and OpenFAST are 20.7 m and 20.9
411 m, respectively. The discrepancy between the heave motions is relatively smaller than the

difference in the surge motion. The heave motion predicted by the coupled model developed in AQWA is almost identical with the result obtained using OpenFAST. The agreement between AQWA and OpenFAST is reasonably good in predicting the platform pitch motion. The results predicted by these two tools follow the same trend over the simulation, although minor differences are observed. The average platform pitch motions from AQWA and OpenFAST are 4.24 degrees and 4.33 degrees, respectively. The relative difference is around 1.92%. The differences between the results are mainly attributed to the mooring system and hydrodynamic loads. Each mooring line is modelled as a quasi-static catenary in OpenFAST, while the mooring lines are modelled using a dynamic approach in AQWA to examine the dynamic effects of the platform motions. In addition, some differences between these two tools in predicting hydrodynamic loads exist. For example, the duration of the convolutional integral used to calculate the radiation force due to memory effect is 120 s in AQWA, while the memory duration in OpenFAST is 60 s by default. Nonetheless, the differences between the platform motions obtained using AQWA and OpenFAST are negligible.

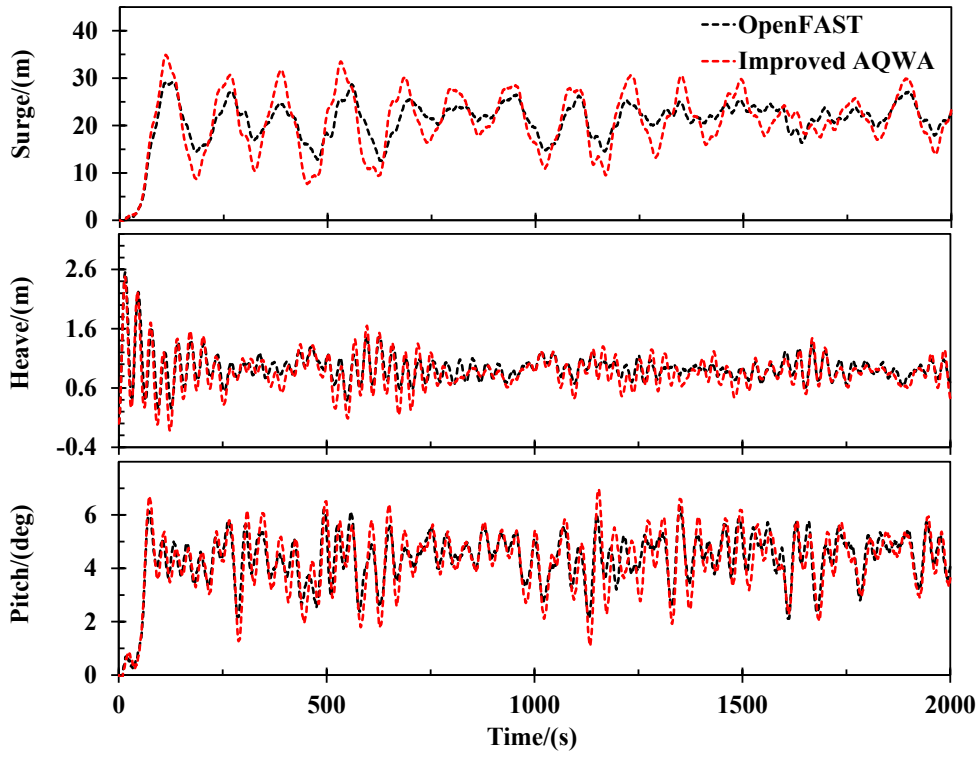

Fig. 5: Comparison between platform responses obtained using OpenFAST and the present coupled model developed in AQWA.

Fig. 6 presents the fairlead tension of each mooring line obtained using OpenFAST and the present coupled model developed in AQWA. The agreement between the fairlead tensions predicted by these two tools is good for each of the mooring lines. The small discrepancy is attributed to the difference in modelling the mooring lines in AQWA and OpenFAST. Each mooring line is modelled as a quasi-static catenary in OpenFAST, while the mooring lines are modelled as dynamic catenaries in AQWA. The dynamic effects due to platform motions are examined in AQWA. Consequently, the tension in each mooring line predicted by AQWA fluctuates in a relatively larger range compared to the results obtained using OpenFAST. Nonetheless, the differences between the mooring tensions obtained using AQWA and OpenFAST are acceptable. The comparisons against OpenFAST indicate that the aero-hydro-servo-elastic model that has been well implemented within AQWA is capable of accurately predicting coupled responses of the FWT. The DLL is capable of performing a fully coupled analysis in AQWA and it has been released to the public on an open source platform, GitHub, as shown in Appendix B.

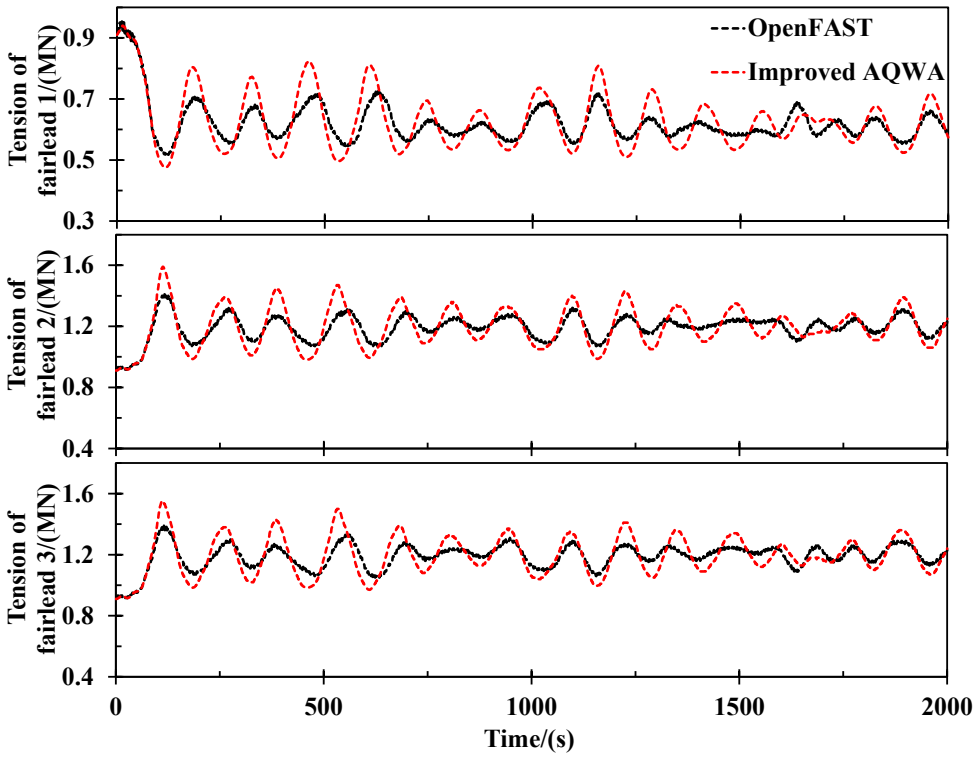

Fig. 6: Fairlead tension of each mooring line predicted by OpenFAST and the present coupled model developed in AQWA.

4.2 Credibility in evaluating hydrodynamic performance of the tidal turbine

The model tests conducted by Bahaj *et al.* [38] and Doman *et al.* [39] are used to validate the numerical tool integrated within AQWA. Fig. 7 presents the comparisons between the test data and numerical results for two different tidal turbines. It is observed that the power and thrust coefficients predicted in the present numerical simulations follow the same variation trends as the data from model test 1, although the numerical simulation slightly overestimates the power coefficient at a high tip speed ratio (TSR). In the model test 2, the numerical results are slightly higher than the test data for low TSRs. In the common operational range of TSR between 4 and 6, the power and thrust coefficients predicted by the numerical model agree well with the test results in both magnitude and variation trend. The overall agreements between the results of the numerical simulations and model tests are reasonably good. The comparisons have confirmed the accuracy of the numerical model in predicting responses of tidal turbines.

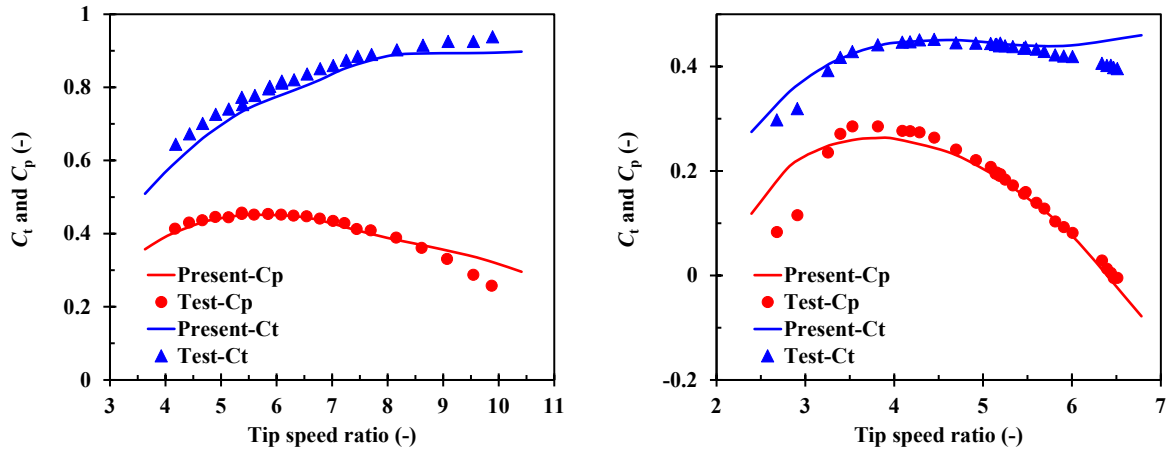

460

461 (a) Model test 1 (b) Model test 2

462 Fig. 7: Comparison between tidal turbine responses obtained from the present numerical

463 simulations and model tests; (a) model test 1 conducted by Bahaj *et al.* [38] for a 0.8 m

464 diameter rotor, (b) model test 2 conducted by Doman *et al.* [39] for a 0.762 m diameter rotor.

465

466 For each inflow current speed within the operational range, a simulation with a duration

467 of 800 s is conducted. The first 200 s transient results are removed and the results of the last

468 600 s are used to obtain the average power and rotor speed. Fig. 8 presents the comparisons

469 between the power and rotor speed predicted by the numerical model and the design parameters

470 versus inflow current speed. It is observed that the numerical results are identical to the design

471 parameters for each inflow current speed. The comparison indicates that the controller

472 implemented in this study is efficient in adjusting rotor speed and blade pitch to achieve a target

473 power.

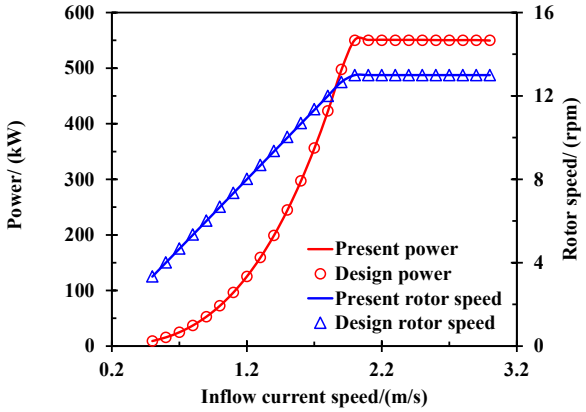

Fig. 8: Comparisons of power and rotor speed under steady conditions

5 Results and Discussions

In this section, the performance of the IFES is evaluated and compared against a single FWT for below-rated, rated and over-rated conditions with regards to the responses of the blades, platform and mooring system. In addition, the power production of these two floating energy systems are compared to highlight the advantage of the IFES concept.

5.1 Load case definition

Based on the met-ocean data of a specific site over the west coast of USA [42], three typical load cases (LCs) are defined. The average wind speeds at the height of 90 m above the MSL are 8 m/s, 11.4 m/s and 16 m/s, respectively, for the three LCs. The corresponding wave properties and current speed at the MSL are presented in Table 4. It is noted that the rated current speed of the tidal turbine is 2 m/s which is much larger than the current speed examined in this study. It is anticipated that the additional power production of the tidal turbines will be less than their rated power. The full-field turbulent winds are generated using TurbSim [43] based on the Kaimal spectrum. A power-law profile with an exponent of 0.12 is adopted to examine the wind shear effect. Fig. 9 presents the generated wind field with an average speed of 11.4 m/s at the hub height. The kinematics of the irregular waves are generated based on the

493 P-M spectrum in AQWA. The current speed distribution along the water depth follows a
494 power-law profile with an exponent of 1/7 as suggested [32]. The dynamic responses of the
495 IFES and FWT are examined for each load case. The simulation length is 4600 s and the time
496 step is 0.005 s.

497 Table 4: Environmental conditions of the load cases

Load case	Wind speed at hub height (m/s)	Significant height (m)	Spectral peak period (s)	Current speed at the MSL (m/s)
LC1	8.0	1.316	8.006	1.0
LC2	11.4	1.836	7.441	1.1
LC3	16.0	2.598	7.643	1.2

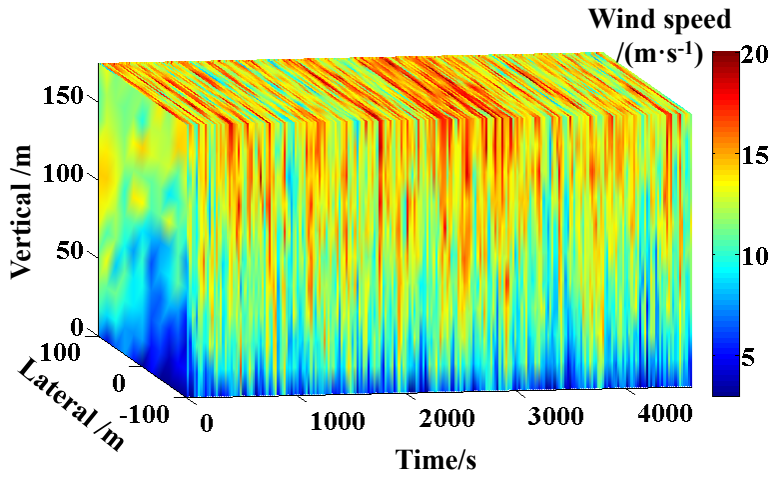

498
499 Fig. 9: Wind field with an average speed of 11.4 m/s at the hub height
500

501 ## *5.2 Blade responses*

502 The out-of-plane (OoP) blade-tip deflection and rotor thrust of the present IFES concept
503 and a single FWT under LC2 are presented in Fig. 10. The time domain variations of the rotor
504 thrust of the IFES follows the same trend as the result of the FWT. The difference in magnitude
505 is negligible. Similar phenomenon is observed for the blade-tip deflection. The results indicate
506 that the tidal turbines attached to the spar platform have insignificant effects on the
507 aerodynamic performance of the wind turbine.

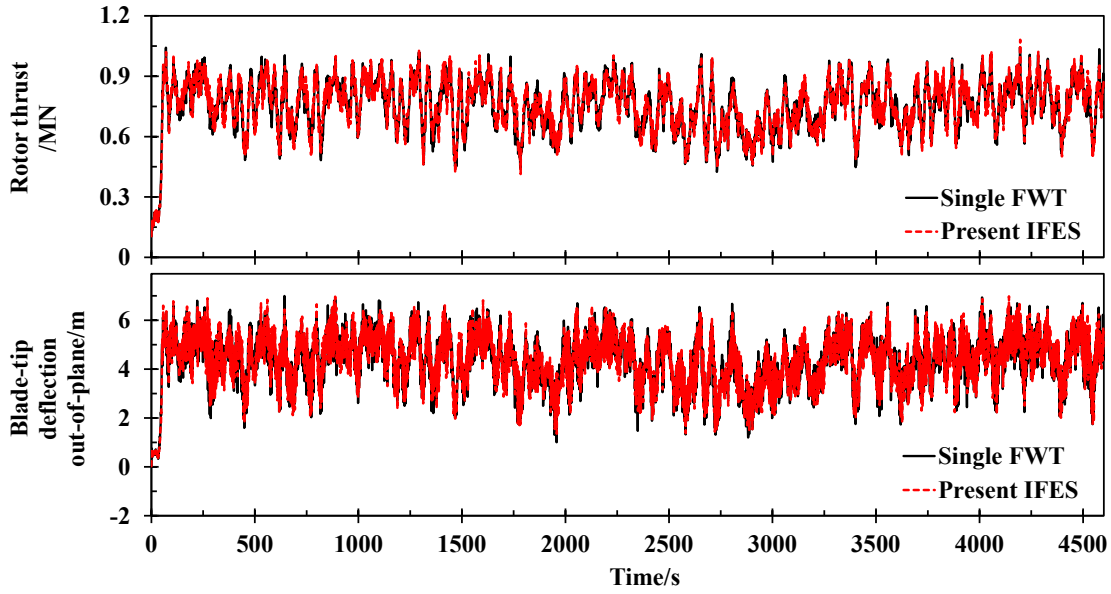

Fig. 10: Blade-tip deflection and rotor thrust under LC2

Table 5 presents the statistics of the blade-tip deflection and rotor thrust of the single FWT and IFES under the three LCs. The maximum blade-tip deflection of the IFES under LC1 is 1.1% smaller than that of the FWT, the corresponding standard deviation is 1.28% larger. Similar phenomenon is observed for the rotor thrust. It is noted that the errors between the statistical responses of the IFES and FWT are smaller than 2% for all the LCs, which include the below-rated and over-rated conditions. The aero-elastic responses and aerodynamic performance of the IFES are similar to those of the FWT. The statistical results imply that the influence of the tidal turbines on the dynamic responses of the rotor is weak. It is anticipated that the installation of additional tidal turbines on the spar platform has negligibly negative effects on the dynamics and performance of the blades.

Table 5: Statistics of the OoP blade-tip deflection and rotor thrust (during 400 s ~ 4600s)

		Blade-tip deflection (OoP)/m			Rotor thrust/kN		
		IFES	FWT	Error	IFES	FWT	Error
LC1	Max	4.58	4.63	-1.10%	733.8	747.7	-1.86%
	Mean	3.27	3.28	-0.20%	554.5	554.5	-0.01%
	Std.dev	0.39	0.38	1.28%	57.7	58.6	-1.44%
LC2	Max	7.00	7.05	-0.62%	1036.0	1052.0	-1.52%
	Mean	4.47	4.45	0.51%	769.1	765.0	0.53%

	Std.dev	0.97	0.99	-1.42%	114.7	117.0	-1.99%
	Max	6.27	6.12	2.42%	1029.0	1016.0	1.28%
LC3	Mean	2.49	2.47	0.82%	558.5	553.5	0.90%
	Std.dev	1.01	1.00	0.92%	95.9	94.7	1.32%

522

523 ### *5.3 Platform responses*

524 The platform responses of the IFES and the single FWT under LC2 are presented in Fig.
525 11. Significant differences between the platform motions of the IFES and FWT are observed.
526 The average value of the surge motion of the IFES is significantly larger, while the fluctuation
527 is much smaller compared to the surge motion of the single FWT. This is because the tidal
528 turbines provide a considerable thrust when the wind turbine moves towards the inflow wind.
529 The hydrodynamic thrusts produced by the tidal turbines act as a damping against the wind
530 turbine when moving towards the upwind direction. The presence of the tidal turbines improves
531 the transient behavior of the platform which is caused by the rapid decrease of aerodynamic
532 damping when the controller increases the blade pitch angle under an over-rated condition.

533 The platform heave of the IFES is smaller than the heave of the FWT. This means that the
534 equilibrium position of the IFES is lower since the buoyancy provided by the tidal turbines is
535 smaller than their weights. Relatively small discrepancy in the pitch motions of the IFES and
536 FWT is observed. The contribution by the tidal turbines to the platform pitch motion is
537 negligible since the pitch motion is mainly influenced by the wind loading. As indicated by the
538 results presented in Fig. 10, the tidal turbines have insignificant effects on the aerodynamic
539 loads of the wind turbine, although they have notable effects on the platform surge that is
540 coupled with aerodynamic loads. However, the velocity variation of the turbulent wind in LC2
541 is still the main contribution to the fluctuation of relative inflow speed of the wind turbine.
542 Therefore, the pitch motion dominated by the wind loading is weakly affected by the tidal
543 turbines.

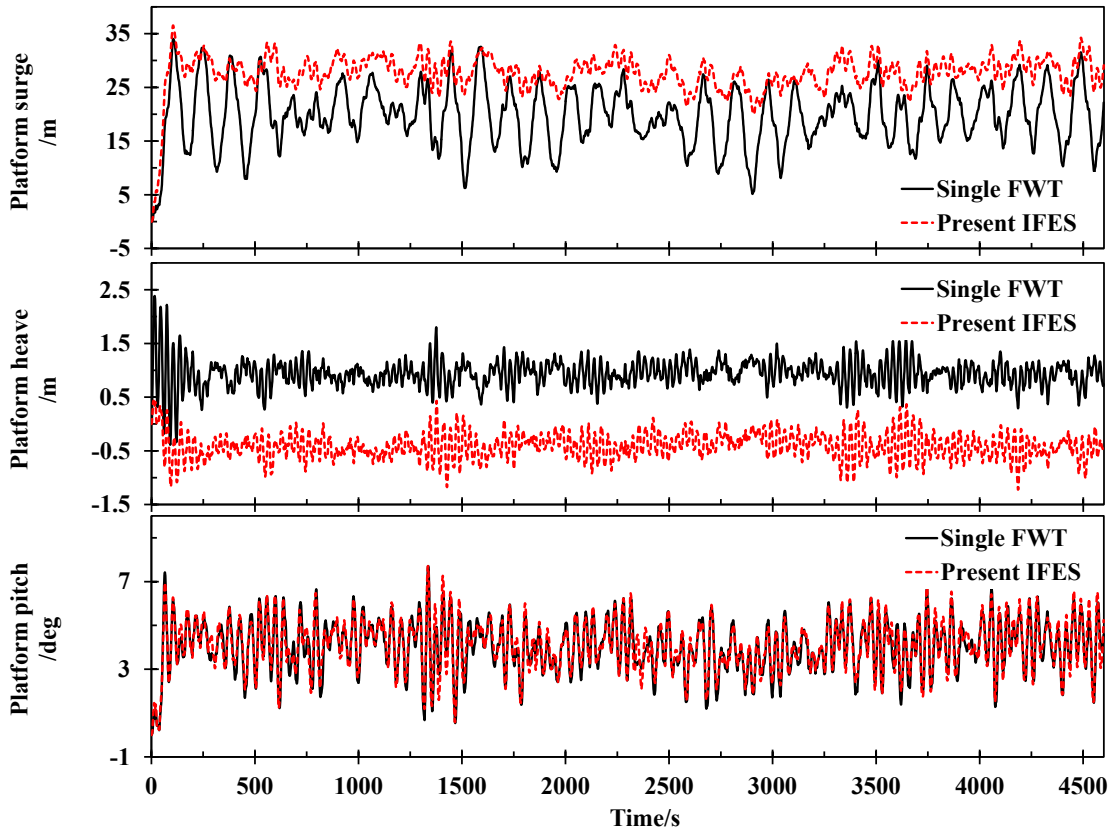

Fig. 11: Platform motions of the IFES and FWT under LC2.

By applying a Fast Fourier Transformation (FFT) on the time series of the platform responses under LC2, the spectral responses of the platform are obtained as presented in Fig. 12. As observed from Fig. 12(a), the surge amplitude corresponding to the natural frequency of the surge mode of the IFES is much smaller than that of the FWT. It means that the response from the surge mode is significantly mitigated by the tidal turbines. The contribution of the surge mode to the heave motion is also reduced as indicated by Fig. 12(b). It is noted that the discrepancy in the amplitudes at other frequencies of the IFES and FWT is insignificant. Since the platform pitch is mainly influenced by the wind loading, the spectral responses of the platform pitch of the IFES and FWT are similar.

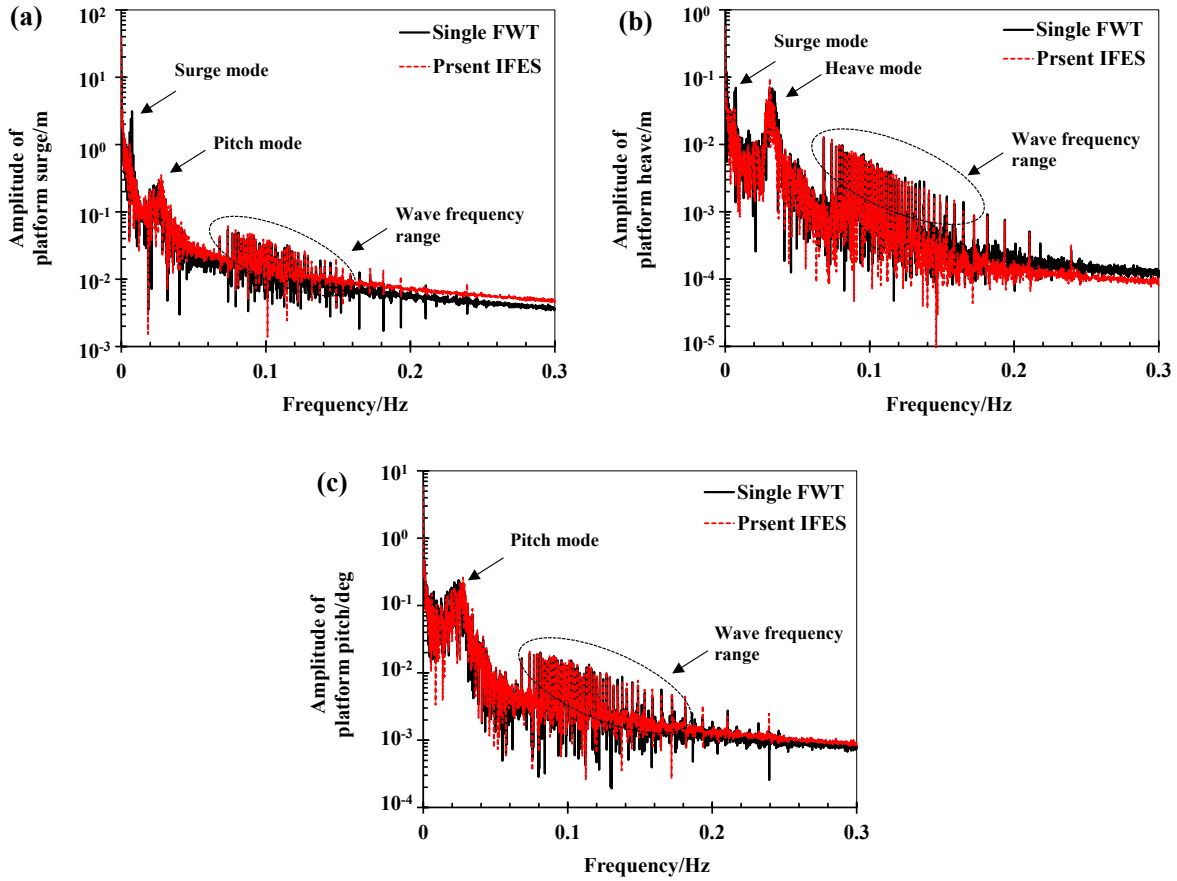

Fig. 12: Spectral responses of the platform under LC2. (a) surge, (b) heave and (c) pitch.

The statistical results of the platform motions are given in Table 6. Similar to the results under LC2, the maximum surge motion of the IFES is larger than that of the FWT under both LC1 and LC3 due to the additionally considerable thrusts produced by the tidal turbines. For the same reason, the standard deviations are smaller. Under LC1, the surge standard deviations of the IFES and FWT are 1.55 m and 2.49 m, respectively. It means that the tidal turbines mitigate the surge fluctuation by 37.5%. Reductions of 57.2% and 42.1% on the surge standard deviation are achieved under LC2 and LC3, respectively. It is anticipated that the fluctuation of the tension in a mooring line will decrease due to the tidal turbines under all the LCs.

Table 6: Statistical platform responses of the IFES and FWT (during 400 s ~ 4600s)

	Surge/m	Heave/m	Pitch/degree

		IFES	FWT	IFES	FWT	IFES	FWT
	Max	24.67	19.93	0.136	1.395	4.162	4.137
LC1	Mean	20.49	13.72	-0.114	1.129	2.877	2.802
	Std.dev	**1.55**	**2.49**	0.101	0.095	0.419	0.448
	Max	33.54	32.58	0.436	1.803	7.709	7.705
LC2	Mean	28.13	20.02	-0.425	0.926	4.171	4.101
	Std.dev	**2.29**	**5.36**	0.217	0.212	1.151	1.207
	Max	30.30	23.66	0.446	1.850	6.510	6.331
LC3	Mean	23.57	13.67	-0.200	1.117	3.026	2.842
	Std.dev	**1.90**	**3.27**	0.226	0.212	1.182	1.112

5.4 Tension in mooring lines

Fig. 13 presents the fairlead tension of each mooring line of the IFES and FWT under LC2. As expected, the fluctuation of tension in the mooring lines of the IFES is smaller than that of the FWT due to the smaller variation range of the surge motion. As the IFES suffers an additionally considerable thrust generated by the tidal turbines, its equilibrium position is relatively farther than that of the FWT. Consequently, compared with the single FWT, the mooring line #1 placed in the downwind direction is in a looser state, while the stretched lengths of the upwind mooring lines (#2 and #3) are larger. As a result, the mean tension in mooring line #1 of the IFES is smaller compared to the results of the FWT, while the mooring lines #2 and #3 have a larger average tension.

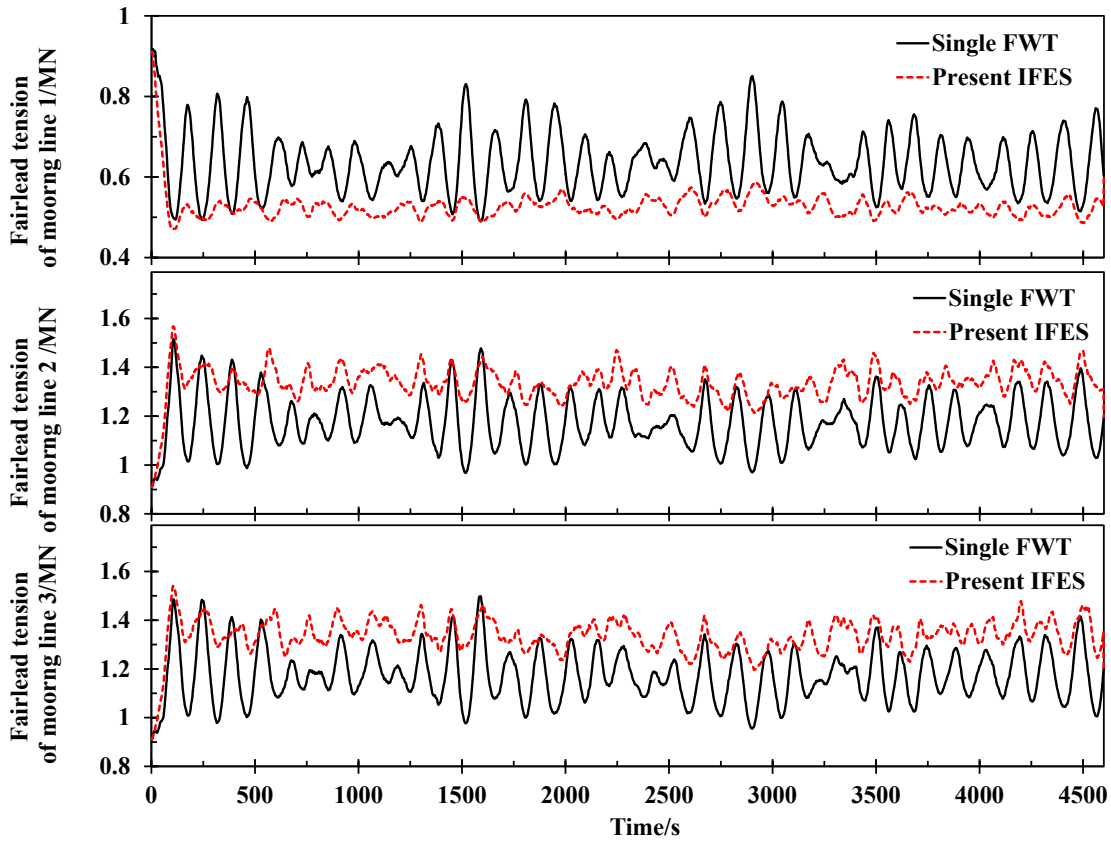

Fig. 13: Fairlead tension in the mooring lines of the IFES and FWT under LC2

The mean values and standard deviations of the fairlead tension in the mooring lines of the IFES and FWT under all the three LCs are presented in Table 7. Similar to the results under LC2, the average tension in mooring line #1 of the IFES is smaller than that of the FWT under both LC1 and LC3. In addition, the standard deviation of the tension in mooring line is significantly decreased by the tidal turbines. For the upwind mooring lines, the mean tension increases and the standard deviation of the tension decreases due to the presence of the tidal turbines. More specifically, the mean tensions in mooring line #2 of the IFES and FWT under LC 1 are 1196.0 kN and 1083.2 kN, respectively. The corresponding standard deviations of the tensions are 28.1 kN and 40.3 kN, respectively. The mean tension increases by 10.4% while the standard deviation decreases by 30.4%. Similar phenomena are observed for LC2 and LC3. The enhancements on the mean tension in mooring line #2 under LC2 and LC3 are 162.9 kN

595 and 177.7 kN, respectively, equivalent to increase of 13.8% and 16.3%. Meanwhile, the
596 standard deviations of the tension in mooring line #2 under LC2 and LC3 decrease by 53.3%
597 and 39.3%, respectively. The statistical results indicate that the load in a downwind mooring
598 line is mitigated, while the loads in the upwind mooring lines are enhanced by the tidal turbines.
599 It is anticipated that the service lifetime of the downwind mooring line will be extended due to
600 the smaller mean load and fluctuation. However, the influence on the fatigue damage of the
601 upwind mooring lines requires a further investigation, since the mean value of the tension
602 increases but the standard deviation significantly decreases.
603
604 Table 7: Mean value and standard deviation of the fairlead tension of the mooring lines

		Mooring line #1/kN		Mooring line #2/kN		Mooring line #3/kN	
		IFES	FWT	IFES	FWT	IFES	FWT
LC1	Mean	593.1	700.9	1196.0	1083.2	1196.4	1082.9
	Std.dev	16.4	38.8	28.1	40.3	28.1	41.3
LC2	Mean	522.9	632.2	1340.7	1177.8	1346.0	1180.6
	Std.dev	17.3	72.3	49.2	105.4	49.7	103.5
LC3	Mean	557.7	703.7	1265.3	1087.6	1256.0	1077.1
	Std.dev	13.5	50.1	33.2	54.7	33.6	54.7

605

606 ## *5.5 Power production*

607 The generator power of the IFES and FWT under LC2 is presented in Fig. 14. As indicated
608 in the previously presented results, the tidal turbines have a slight influence on the aerodynamic
609 performance of the wind turbine. Therefore, the generator power of the IFES contributed by
610 the wind turbine is similar to that of the single FWT. The average generator powers of the IFES
611 and FWT are 4773.7 kW and 4777.2 kW, respectively. The inflow current speed at the MSL is
612 1.1 m/s in LC2. It means that the constant inflow current speed at the depth of 46.5 m is 1.08
613 m. The corresponding design power of the tidal turbine is 88.4 kW. The dynamic inflow due
614 to the platform motions affects the actual generator power of the tidal turbines. The average
615 power of the two tidal turbines is 183.2 kW that is slightly higher than the target design power.

Compared to a single FWT, the average output power is increased by 3.84% due to the presence of the tidal turbines under LC2.

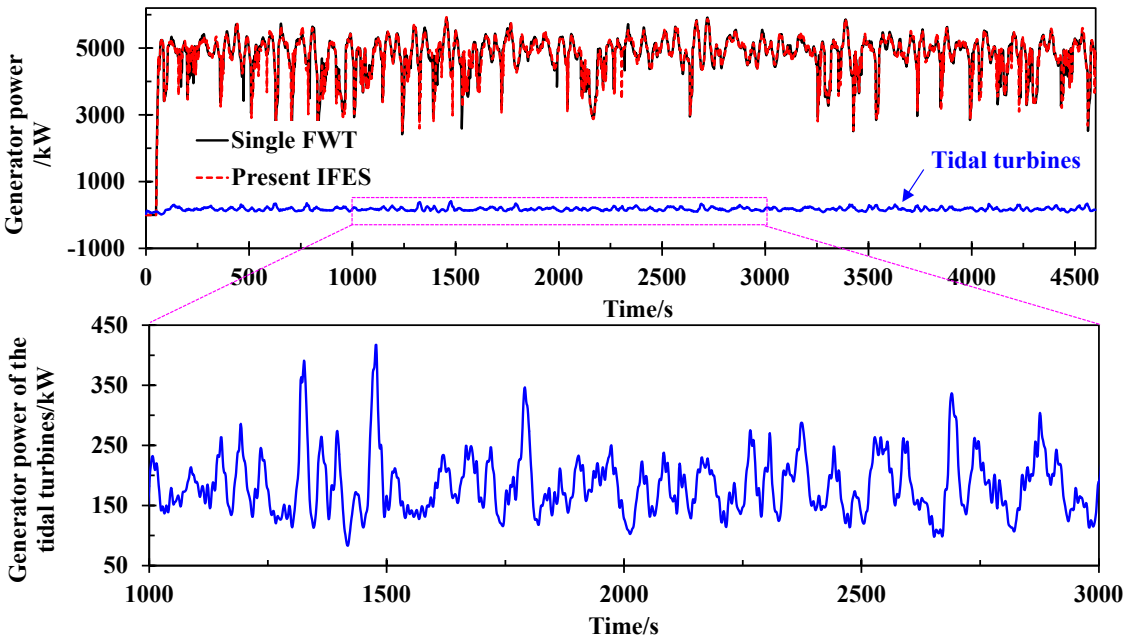

Fig. 14: Generator power of the IFES and FWT under LC2

The presence of the tidal turbines has a slight influence on the power production of the wind turbine for the examined LCs, as indicated by Table 8. The results indicate that the total power production is increased by 3.84% to 6.46% due to additional tidal turbines. Although the wind power of the IFES is decreased by 10.1 kW compared to the single FWT, the tidal turbines provides an additional power production of 135.1 kW. As a result, the total power of the IFES is increased by 6.46%. It is also found that the total power production increases by 237 kW under LC3, equivalent to an enhancement of 4.74%.

Table 8: Average power of the wind and tidal turbines under the examined LCs

	IFES/kW			FWT/kW	Error
	Wind	Tidal	Total	Total	
LC1	1923.1	135.1	2058.2	1933.2	6.46%
LC2	4773.7	183.3	4957.0	4777.2	3.84%
LC3	4998.9	237.0	5235.9	4998.7	4.74%

The average power output of the FWT and IFES including the contributions of the tidal turbines under the three LCs are presented in Fig. 15. The average power generation of the IFES is higher than the one of the FWT for each LC. It means that the tidal turbine is beneficial in enhancing the total power production of the floating wind energy system.

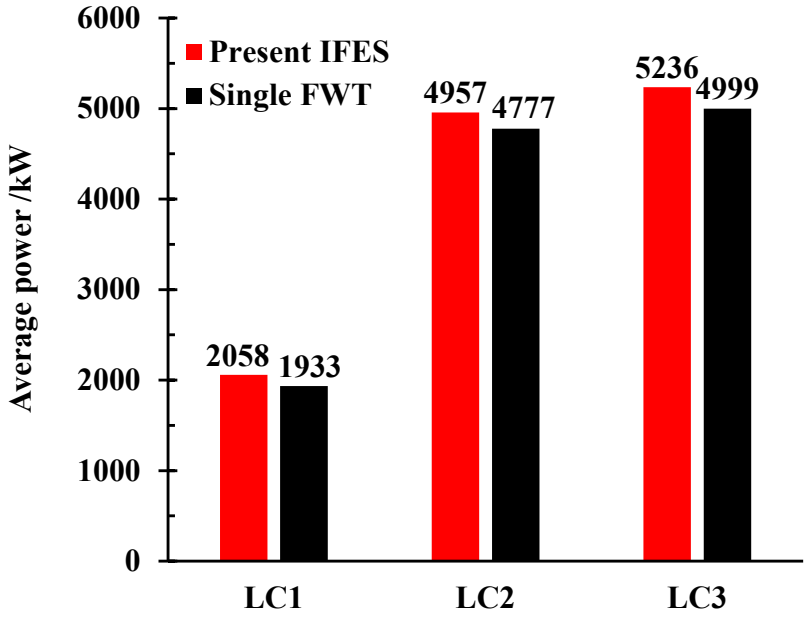

Fig. 15: Average power outputs of the IFES and FWT under the three LCs

6 Conclusions

This study proposed an integrated floating energy system by combining two 550 kW tidal turbines with a 5 MW wind turbine supported by a spar platform. A novel fully coupled numerical tool is developed by implementing the aero-servo-elastic simulation capabilities within the commercial hydrodynamic analysis software package, AQWA. In addition, the AeroDyn program is integrated with the coupled tool to evaluate performance of the tidal turbines. A torque-pitch controller is implemented within the coupled tool for the tidal turbines operating under dynamic inflow conditions due to the platform motions. Numerical results

from OpenFAST and experimental data from model tests are used to verify the accuracy of the fully coupled model in predicting dynamic responses of a FWT and tidal turbines. The aerodynamic performance of the rotor, and dynamic responses of the blade, platform and mooring system of the IFES under different LCs are obtained using the coupled tool. The main conclusions of this study are listed as follows:

(1) A novel fully coupled aero-hydro-servo-elastic tool based on AQWA and AeroDyn program is developed for dynamic analysis of the IFES concept. The comparisons against OpenFAST and model tests have validated the accuracy of the coupled tool in predicting dynamic responses of a hybrid floating energy concept subjected to wind and wave loadings. The DLL is capable of examining aero-servo-elastic coupled effects of FWTs and it has been released to the public. Details of the open source code can be found in Appendix B.

(2) The tidal turbines have insignificant influences on the blade-tip deflection and rotor thrust of the wind turbine. The transient behavior of the platform is improved due to the presence of the tidal turbines which provide a considerable damping against the wind turbine moving towards the upwind direction. The IFES has similar dynamic responses of blades and aerodynamic performance to those of a single FWT, while the hydrodynamic performance is better.

(3) The downwind mooring line of the IFES has a smaller mean fairlead tension compared to the FWT, while the fluctuation range is much smaller. The fatigue damage is anticipated to be reduced by the presence of the tidal turbines. Although the mean tensions in the upwind mooring lines of the IFES are larger than those of a FWT, the standard deviations are much smaller. The standard deviation of the tension in an upwind mooring line decreases by 30.4% to 53.3% depending on the environmental conditions.

(4) The average power generation of the IFES is higher than the one of the FWT for each of the examined load cases. An enhancement of up to 6.46% is achieved on the overall power

production due to the tidal turbines. The results confirm that the IFES concept is beneficial in enhancing total power production without weakening the dynamic performance of a FWT.

Appendix A: Implementation of the controller for the tidal turbine

This study employs the control algorithm developed by Jonkman for the NREL 5 MW wind turbine in implementing the torque-pitch controller for the tidal turbine. The torque-pitch controller consists of a simple partial-load controller and a proportional-integral (PI) controller. The partial-load controller defines the torque-speed curve when the output power is smaller than the rated power as shown in Fig. 16. The gearbox ratio is assumed to be 1 for simplicity.

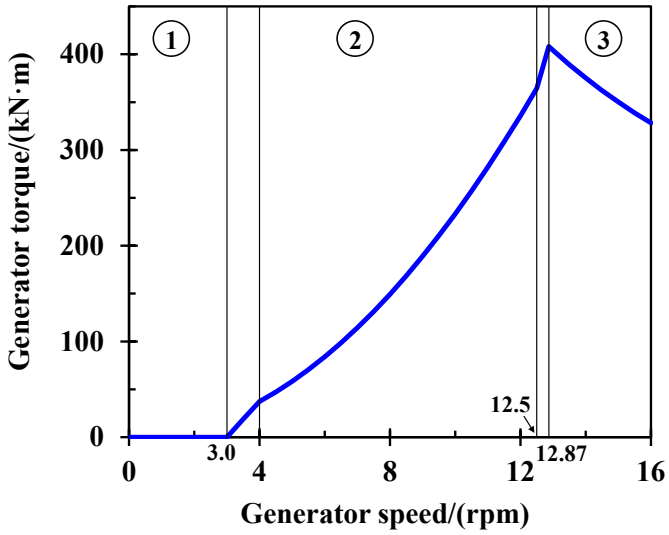

Fig. 16: Torque versus rotor speed of the controller

In region 1, the generator torque is 0. The cut-in rotor speed for outputting power is chosen as 3 rpm. In region 2, the torque is equal to the square of the generator speed. The tidal turbine operates in its best TSR of 6.98. The quadratic coefficient is 2333.4 Nm/(rpm)^2. The starting and ending limits of region 2 are chosen as 4 rpm and 12.5 rpm. The starting generator speed of region 3 is selected as 99% of the rated speed. Once the generator speed exceeds the limit, the PI controller takes over in region 3 where the target output power remains constantly being the rated power.

688 In region 3, a PI controller is activated to adjust blade pitch angle as follows:

689 $$\Delta\theta = K_P \Delta\Omega + K_I \int_0^t \Delta\Omega \mathrm{d}t \tag{22}$$

690 where $\Delta\theta$ and $\Delta\Omega$ are the perturbations of the blade pitch angle and generator speed; K_P

691 and K_I are the proportional and integral gains, respectively.

692 Based on the power performance of the tidal turbine, K_P and K_I corresponding to 0

693 degree blade pitch are obtained with values of 39.42 rad·s/rad and 16.89 rad/rad, respectively.

694 The linear adjustment coefficient η of the PI gains for a specific blade pitch angle θ is given

695 as:

696 $$\eta = 1 \big/ \left(1 + \theta/\psi\right) \tag{23}$$

697 where ψ is 0.00345 rad.

698 The main parameters of the controller are given in Table 9. Fig. 17 presents the generator

699 power, rotor speed and blade pitch of the tidal turbine under an unsteady inflow condition. The

700 inflow current speed increases gradually from 0.5 m/s to 3.0 m/s over the simulation. The

701 results shown in Fig. 17 indicate that the controller implemented in this study is effective to

702 adjust rotor speed and blade-pitch of the tidal turbines under dynamic inflow current conditions.

703 Table 9: Main parameters of the controller

Value	Variable	Description
1.570796	CornerFreq	Corner frequency (-3dB point) in the low-pass filter, rad/s.
0.0001	PC_DT	Communication interval for pitch controller, s.
16.89436	PC_KI	Integral gain for pitch controller at rated pitch (zero), (-).
0.003452	PC_KK	Gains adjustment coefficient.
39.42017	PC_KP	Proportional gain for Pitch controller at rated Pitch (zero), s.
1.570796	PC_MaxPit	Maximum pitch setting in pitch controller, rad.
0.139626	PC_MaxRat	Maximum pitch rate (in absolute value) in pitch controller, rad/s.
0.0	PC_MinPit	Minimum pitch setting in pitch controller, rad.
1.361357	PC_RefSpd	Desired (reference) HSS speed for pitch controller, rad/s.
0.314159	VS_CtInSp	Transitional generator speed (HSS side) between regions 1 and 1 1/2, rad/s.
0.0001	VS_DT	Communication interval for torque controller, s.
80000	VS_MaxRat	Maximum torque rate (in absolute value) in torque controller, N-m/s.
484810.4	VS_MaxTq	Maximum generator torque in Region 3 (HSS side), N-m.
212779.5	VS_Rgn2K	Generator torque constant in Region 2 (HSS side), N-m/(rad/s)^2.
0.418879	VS_Rgn2Sp	Transitional generator speed (HSS side) between regions 1 1/2 and 2, rad/s.
0.017453	VS_Rgn3MP	Minimum pitch angle in region 3 regardless of the generator speed, rad.
1.347743	VS_RtGnSp	Rated generator speed (HSS side), rad/s.
550000	VS_RtPwr	Rated generator power in Region 3, Watts.
10	VS_SlPc	Rated generator slip percentage in Region 2 1/2, %.

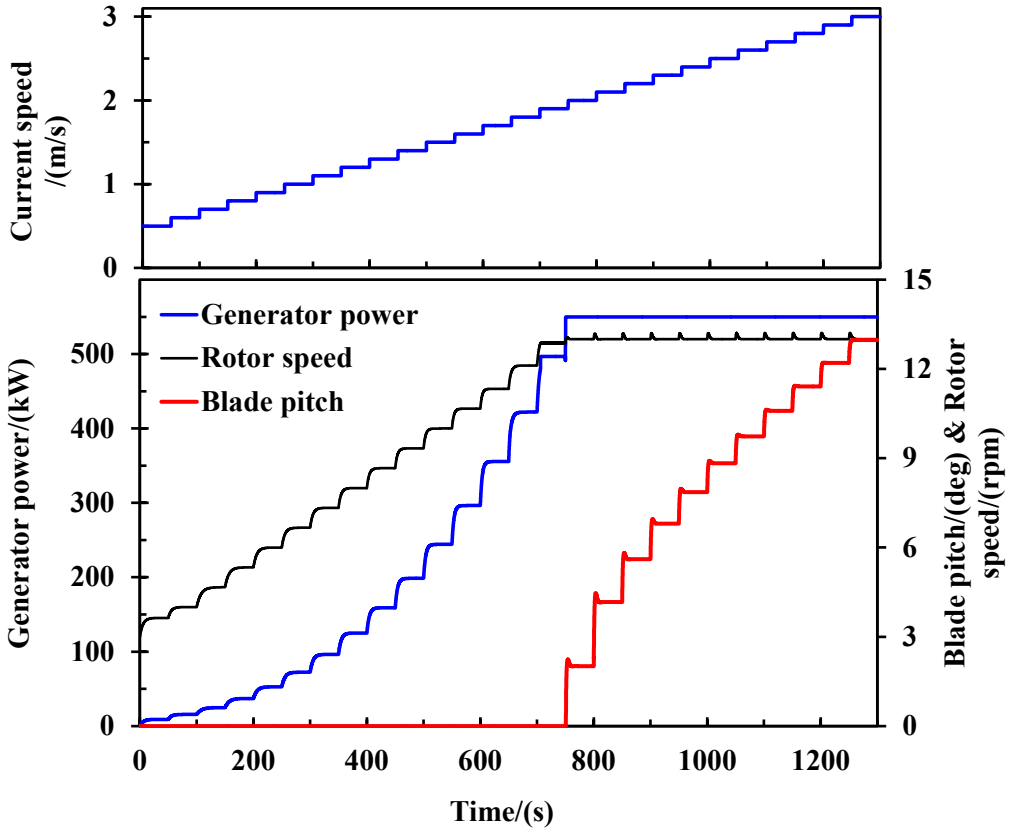

Fig. 17: Controller performance under an unsteady inflow condition

Appendix B: Public release of the fully coupled model

The DLL used in this study, which is capable of performing a fully coupled analysis of FWTs using AQWA, is released to the public on GitHub and can be accessed via the link: https://github.com/yang7857854/F2A. The source code and a user manual of F2A have been uploaded in the repository.

Acknowledgements

This project is funded by European Regional Development Fund (ERDF), Interreg Atlantic Area (grant number: EAPA_344/2016) and the European Union's Horizon 2020 research and innovation programme under the Marie Skłodowska-Curie grant agreement no.

730888 (RESET). The authors would also like to acknowledge the financial support from National Natural Science Foundation of China (grant numbers: 51676131 and 51976131), Science and Technology Commission of Shanghai Municipality (grant number: 1906052200) and Royal Society (grant number: IEC\NSFC\170054).

References

[1] DNV-GL. (2019), Energy transition outlook 2019: A global and regional forecast to 2050. *Det Norske Veritas - Germanischer Lloyd report*, 2019

[2] Driscoll, F., Jonkman, J., Robertson, A., Sirnivas, S., Skaare, B., & Nielsen, F. G. (2016). Validation of a FAST model of the statoil-hywind demo floating wind turbine. *Energy Procedia*, 94(NREL/JA-5000-66650).

[3] Jonkman, J. (2010). Definition of the Floating System for Phase IV of OC3. *National Renewable Energy Laboratory (NREL), Technical report (*No. NREL/TP-500-47535t*)*, Colorado, United States.

[4] Karimirad, M., & Moan, T. (2011). Wave-and wind-induced dynamic response of a spar-type offshore wind turbine. *Journal of waterway, port, coastal, and ocean engineering*, 138(1), 9-20.

[5] Yu, M., Hu, Z. Q., & Xiao, L. F. (2015). Wind-wave induced dynamic response analysis for motions and mooring loads of a spar-type offshore floating wind turbine. *Journal of Hydrodynamics*, 26(6), 865-874.

[6] Yue, M., Liu, Q., Li, C., Ding, Q., Cheng, S., & Zhu, H. (2020). Effects of heave plate on dynamic response of floating wind turbine Spar platform under the coupling effect of wind and wave. *Ocean Engineering*, 201, 107103.

[7] Ahn, H. J., & Shin, H. (2019). Model test and numerical simulation of OC3 spar type floating offshore wind turbine. *International Journal of Naval Architecture and Ocean Engineering*, 11(1), 1-10.

[8] Lin, Y. H., Hsu, C. L., & Kao, S. H. (2019). Hydrodynamics of the wind float OC3-Hywind with mooring loads estimated by the modular system. J*ournal of Marine Science and Technology*, 24(1), 237-248.

[9] Lyu, G., Zhang, H., & Li, J. (2019). Effects of incident wind/wave directions on dynamic response of a SPAR-type floating offshore wind turbine system. *Acta Mechanica Sinica*, 35(5), 954-963.

[10] Robertson, A., Jonkman, J., Masciola, M., Song, H., Goupee, A., Coulling, A., & Luan, C. (2014). Definition of the semisubmersible floating system for phase II of OC4. *National Renewable Energy Laboratory (NREL), Technical report (No. NREL/TP-5000-60601)*, Colorado, United States.

[11] Matha, D. (2010). Model development and loads analysis of an offshore wind turbine on a tension leg platform with a comparison to other floating turbine concepts. *National Renewable Energy Laboratory (NREL), Technical report (No. NREL/SR-500-4589)*, Colorado, United States.

[12] Jonkman, J. M., & Matha, D. (2011). Dynamics of offshore floating wind turbines—analysis of three concepts. *Wind Energy*, 14(4), 557-569.

[13] Yuce, M. I., & Muratoglu, A. (2015). Hydrokinetic energy conversion systems: A technology status review. *Renewable and Sustainable Energy Reviews*, 43, 72-82.

[14] Patel, V., Eldho, T. I., & Prabhu, S. V. (2017). Experimental investigations on Darrieus straight blade turbine for tidal current application and parametric optimization for hydro farm arrangement. *International journal of marine energy*, 17, 110-135.

[15] Patel, V., Eldho, T. I., & Prabhu, S. V. (2019). Performance enhancement of a Darrieus hydrokinetic turbine with the blocking of a specific flow region for optimum use of hydropower. *Renewable Energy*, 135, 1144-1156.

[16] Blackmore, T., Myers, L. E., & Bahaj, A. S. (2016). Effects of turbulence on tidal turbines: Implications to performance, blade loads, and condition monitoring. *International Journal of Marine Energy*, 14, 1-26.

[17] Scarlett, G. T., & Viola, I. M. (2020). Unsteady hydrodynamics of tidal turbine blades. *Renewable Energy*, 146, 843-855.

[18] Bahaj, A. S., Batten, W. M. J., & McCann, G. (2007). Experimental verifications of numerical predictions for the hydrodynamic performance of horizontal axis marine current turbines. *Renewable energy*, 32(15), 2479-2490.

[19] Zhang, L., Wang, S. Q., Sheng, Q. H., Jing, F. M., & Ma, Y. (2015). The effects of surge motion of the floating platform on hydrodynamics performance of horizontal-axis tidal current turbine. *Renewable energy*, 74, 796-802.

[20] Patel, V., Bhat, G., Eldho, T. I., & Prabhu, S. V. (2017). Influence of overlap ratio and aspect ratio on the performance of Savonius hydrokinetic turbine. *International Journal of Energy Research*, 41(6), 829-844.

[21] Patel, V., Eldho, T. I., & Prabhu, S. V. (2018). Theoretical study on the prediction of the hydrodynamic performance of a Savonius turbine based on stagnation pressure and impulse momentum principle. *Energy Conversion and Management*, 168, 545-563.

[22] Muliawan, M. J., Karimirad, M., & Moan, T. (2013). Dynamic response and power performance of a combined spar-type floating wind turbine and coaxial floating wave energy converter. *Renewable Energy*, 50, 47-57.

[23] Wan, L., Gao, Z., & Moan, T. (2015). Experimental and numerical study of hydrodynamic responses of a combined wind and wave energy converter concept in survival modes. *Coastal Engineering*, 104, 151-169.

[24] Michailides, C., Gao, Z., & Moan, T. (2016). Experimental study of the functionality of a semisubmersible wind turbine combined with flap-type Wave Energy Converters. *Renewable Energy*, 93, 675-690.

[25] Michailides, C., Gao, Z., & Moan, T. (2016). Experimental and numerical study of the response of the offshore combined wind/wave energy concept SFC in extreme environmental conditions. *Marine Structures*, 50, 35-54.

[26] Michele, S., Renzi, E., Perez-Collazo, C., Greaves, D., & Iglesias, G. (2019). Power extraction in regular and random waves from an OWC in hybrid wind-wave energy systems. *Ocean Engineering*, 191, 106519.

[27] Hallak, T. S., Gaspar, J. F., Kamarlouei, M., Calvário, M., Mendes, M. J., Thiebaut, F., & Guedes Soares, C. (2018). Numerical and experimental analysis of a hybrid wind-wave offshore floating platform's hull. *In ASME 2018 37th International Conference on Ocean, Offshore and Arctic Engineering*, Madrid, Spain.

[28] Li, L., Gao, Y., Yuan, Z., Day, S., & Hu, Z. (2018). Dynamic response and power production of a floating integrated wind, wave and tidal energy system. *Renewable energy*, 116, 412-422.

[29] Li, L., Cheng, Z., Yuan, Z., & Gao, Y. (2018). Short-term extreme response and fatigue damage of an integrated offshore renewable energy system. *Renewable Energy*, 126, 617-629.

[30] Li, L., Yuan, Z. M., Gao, Y., Zhang, X., & Tezdogan, T. (2019). Investigation on long-term extreme response of an integrated offshore renewable energy device with a modified environmental contour method. *Renewable energy*, 132, 33-42.

[31] Jonkman, J., Butterfield, S., Musial, W., & Scott, G. (2009). Definition of a 5-MW reference wind turbine for offshore system development. *National Renewable Energy Laboratory (NREL), Technical report (No. NREL/TP-500-38060)*, Colorado, United States.

[32] Neary, V. S., Lawson, M., Previsic, M., Copping, A., Hallett, K. C., LaBonte, A., & Murray, D. (2014). Methodology for Design and Economic Analysis of Marine Energy Conversion (MEC) Technologies. *Sandia National Laboratory, Technical report (No. SAND2014-3561C)*, New Mexico, United States.

[33] Moriarty, P. J., & Hansen, A. C. (2005). AeroDyn theory manual. *National Renewable Energy Laboratory (NREL), Technical report (No. NREL/TP-500-36881)*, Colorado, United States.

[34] Jonkman, J. M., Hayman, G. J., Jonkman, B. J., Damiani, R. R., & Murray, R. E. (2015). AeroDyn v15 User's Guide and Theory Manual. *National Renewable Energy Laboratory (NREL)*, Colorado, United States.

[35] Yang, Y., Li, C., Zhang, W., Yang, J., Ye, Z., Miao, W., & Ye, K. (2016). A multi-objective optimization for HAWT blades design by considering structural strength. *Journal of Mechanical Science and Technology*, 30(8), 3693-3703.

[36] Jonkman, J. M. (2003). Modeling of the UAE Wind Turbine for Refinement of FAST {_} AD. *National Renewable Energy Laboratory (NREL), Technical report (No. NREL/TP-500-34755)*, Colorado, United States.

[37] Jonkman, J., & Buhl, M. (2004, January). New developments for the NWTC's fast aeroelastic HAWT simulator. In 42nd AIAA Aerospace Sciences Meeting and Exhibit, Nevada, United States.

[38] Bahaj, A. S., Molland, A. F., Chaplin, J. R., & Batten, W. M. J. (2007). Power and thrust measurements of marine current turbines under various hydrodynamic flow conditions in a cavitation tunnel and a towing tank. *Renewable energy*, 32(3), 407-426.

[39] Doman, D. A., Murray, R. E., Pegg, M. J., Gracie, K., Johnstone, C. M., & Nevalainen, T. (2015). Tow-tank testing of a 1/20th scale horizontal axis tidal turbine with uncertainty analysis. *International Journal of Marine Energy*, 11, 105-119.

[40] Jonkman, J., & Musial, W. (2010). Offshore code comparison collaboration (OC3) for IEA Wind Task 23 offshore wind technology and deployment. *National Renewable Energy Laboratory (NREL), Technical report (No. NREL/* TP-5000-48191*)*, Colorado, United States.

[41] Robertson, A. N., Wendt, F., Jonkman, J. M., Popko, W., Dagher, H., Gueydon, S., ... & Soares, C. G. (2017). OC5 project phase II: validation of global loads of the DeepCwind floating semisubmersible wind turbine. *Energy Procedia*, 137, 38-57.

[42] Stewart, G. M., Robertson, A., Jonkman, J., & Lackner, M. A. (2016). The creation of a comprehensive metocean data set for offshore wind turbine simulations. *Wind Energy*, 19(6), 1151-1159.

[43] Jonkman, Bonnie J. (2009). TurbSim user's guide: Version 1.50. Jonkman, J. M., & Buhl Jr, M. L. (2005). FAST user's guide. *National Renewable Energy Laboratory (NREL), Technical Reports (No. NREL/TP-500-46198)*, Golden, United States.